

Aperture Efficiencies of Impulse Radiating Antennas

C. J. Buchenauer, J. S. Tyo, and J. S. H. Schoenberg
Phillips Laboratory

November, 1997

Abstract

A concept of aperture efficiency is introduced for the purpose of comparing and optimizing the performance of impulse radiating antennas (IRAs). The aperture efficiencies of popular lens and reflector IRAs are computed as the ratios of peak radiated power densities on boresight compared with that produced by an ideal IRA with an aperture of equal area and equal total input power. Loss of aperture efficiency occurs through two distinct mechanisms: from power that falls outside the aperture and is lost; and from nonuniform power and polarization distributions within the aperture. Both loss mechanisms are addressed, and means for increasing efficiencies are identified. Aperture efficiencies approaching 100% are feasible in TEM-horn arrays and similar structures.

Classified for public release
20 May 98
DE 98-399

I. Aperture Efficiency

Impulse radiating antennas are a class of focused aperture antenna that uses a lens or parabolic reflector to convert an outgoing inhomogeneous spherical TEM-wave, propagating on a conically symmetric feedline structure, into a plane wave. For such focused aperture systems, the radiated field on boresight at distance r in the far-field limit is given by¹

$$\vec{E}_{rad}(r, t) = \frac{1}{2\pi r c} \frac{d}{dt} \iint_A \vec{E}(x, y, t - r/c) dx dy, \quad (1.1)$$

where $c = 1/\sqrt{\mu\epsilon}$ is the speed of light in the external medium, and the surface integral over the field distribution $\vec{E}(x, y, t)$ covers the planar aperture of area A lying just outside the antenna in the external medium. A well known property of focused aperture antennas is that they achieve the highest gain when the aperture is uniformly illuminated with uniform polarization.² Thus, the aperture of our ideal reference antenna is illuminated with a uniform field \vec{E}_0 , and Eq. 1.1 for this antenna becomes

$$\vec{E}_{rad}(r, t) = \frac{A}{2\pi r c} \frac{d}{dt} \vec{E}_0(t - r/c). \quad (1.2)$$

To make a proper comparison between test and reference antennas, both must have certain parameters in common. They must share the same external medium or media with the

same wave impedance Z_{med} and speed of light c , the distance r to the point of measurement must be the same, they must have the same aperture area A , and they must have the same input drive waveform $f(t)$ and input drive power $P(t)$. The total antenna input power for the test antenna described by Eq. 1.1 is related to the input voltage $V_{in}(t)$ and feedline impedance Z_{line} by

$$P_{in}(t) = \frac{V_{in}^2(t)}{Z_{line}}. \quad (1.3)$$

The total input power for the ideal reference antenna is taken to be the power incident upon the aperture. The reference-antenna input power is then

$$P_{in^*}(t) = A \frac{E_0^2(t)}{Z_{med}}, \text{ with } Z_{med} = \sqrt{\frac{\mu}{\epsilon}}. \quad (1.4)$$

For both antennas to be driven by the same waveforms, all pertinent quantities must be proportional to the same function of time $f(t)$, that is

$$V_{in}(t) = V_0 f(t), \bar{E}_0(t) = \bar{E}_0 f(t), \text{ and } \iint \bar{E}(x, y, t) dx dy = \iint \bar{E}(x, y) dx dy f(t), \text{ for } t \ll \sqrt{A}/c. \quad (1.5)$$

Equation 1.5 holds only for early times, before edge effects can propagate inward and modify the aperture fields. What lies outside the aperture is critical to what occurs later in time. To obtain consistent results, we are restricted to comparing only the prompt responses of different antennas.

We define the prompt aperture efficiency η_A to be the ratio of radiated power density on boresight due to the test antenna to that of an equivalent ideal reference antenna with the parameter constraints described above. Equating Eqs. 1.3 and 1.4 and combining Eqs. 1.1 through 1.5, the prompt aperture efficiency then becomes

$$\eta_A = \frac{E_{rad}^2(r, t)}{E_{rad^*}^2(r, t)} = \frac{1}{A} \frac{Z_{line}}{Z_{med}} \left[\frac{1}{V_{in}} \iint_A E_y(x, y) dx dy \right]^2, \quad (1.6)$$

where, without loss of generality, the y -axis is chosen parallel to the principal component of polarization, and $E_y(x, y)$ is the principal component of the prompt aperture field distribution for an applied antenna input voltage V_{in} . Another convenient way of expressing Eq. 1.6 is

$$\eta_A = \frac{A}{V_{in}^2} \frac{Z_{line}}{Z_{med}} \langle E_y \rangle^2 = \left[\frac{A \langle E_y^2 \rangle}{Z_{med}} \right] / \left[\frac{V_{in}^2}{Z_{line}} \right] \left[\frac{\langle E_y \rangle^2}{\langle E_y^2 \rangle} \right], \text{ with } \langle E_y^k \rangle = \frac{1}{A} \iint_A E_y^k(x, y) dx dy, \quad (1.7)$$

where $\langle E_y^k \rangle$ is the average value of the k 'th power of the y -component of the E-field over the aperture. The first term in brackets in Eq. 1.7 is exactly equal to the fraction of the total input power passing through the aperture in the y -component of the field. The second term in brackets in Eq. 1.7, which is always less than or equal to one by Schwarz's inequality, is due solely to the inhomogeneity in the distribution of the y -component of the E-field within the aperture. This second term is unity only for a uniform E-field distribution.

For apertures and feed electrodes with a well defined width W , as shown in Fig. 1.1, the prompt aperture efficiency simply reduces to

$$\eta_A = \frac{1}{A} \frac{Z_{line}}{Z_{med}} \left[\int_0^W dx \frac{1}{V_{in}} \int_{y_1(x)}^{y_2(x)} dy E_y(x, y) \right]^2 = \frac{1}{A} \frac{Z_{line}}{Z_{med}} \left[\int_0^W dx \right]^2 = \frac{W^2}{A} \frac{Z_{line}}{Z_{med}}. \quad (1.8)$$

Transmission-Line Impedance = Z_{line}
 Wave or Medium Impedance = Z_{med}
 Aperture Efficiency: $\eta_A = [W^2/\Lambda] [Z_{line}/Z_{med}]$
 Transmit Response: $E_{ind} = W [2\pi c]^{-1} [d/dt] V_{in}$
 Receive Response: $V_{out} = W [Z_{line}/Z_{med}] E_{rec}$
 Limited to Early Times: $\Lambda/W/c \gg t \ll W/c$

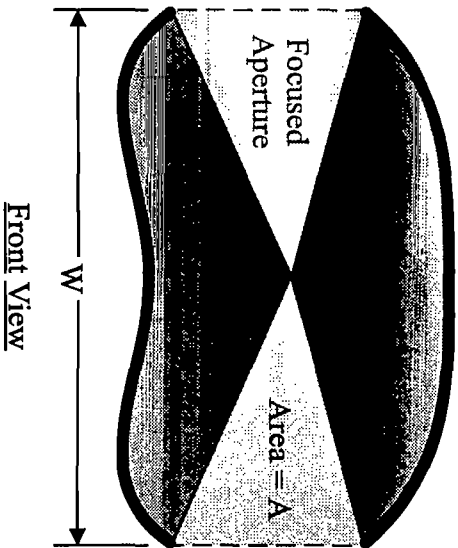


Figure 1.1. Aperture geometry, prompt aperture efficiency, transmission response, and receiving response of focused aperture antennas with a well defined feed-electrode and aperture width W .

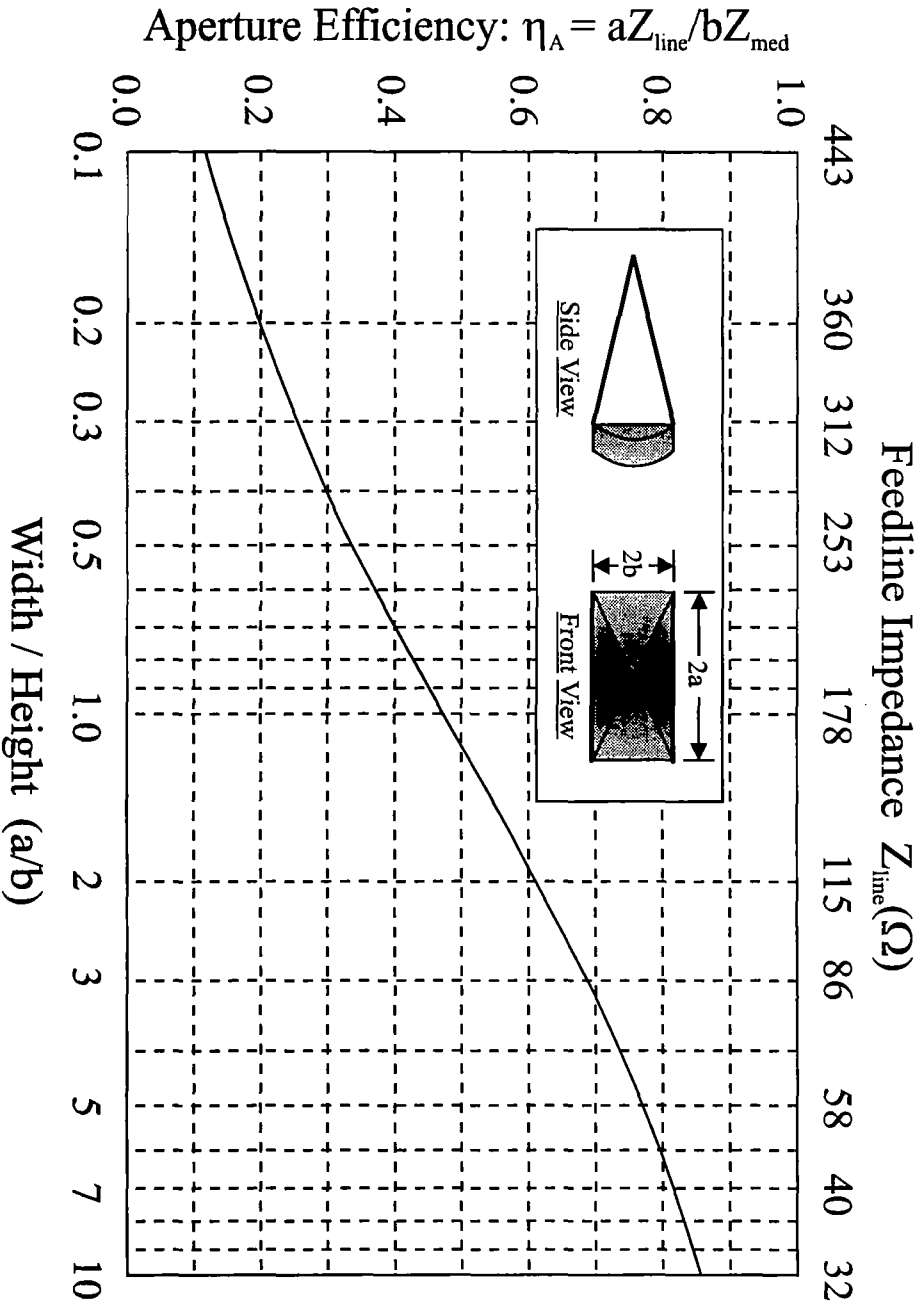


Figure 1.2. Prompt aperture efficiency versus impedance and aspect ratio of flat-plate horns with narrow rectangular focused apertures. Low-impedance horns yield the highest aperture efficiencies.




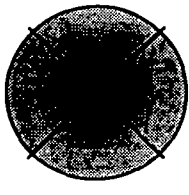
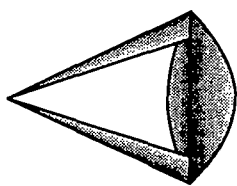

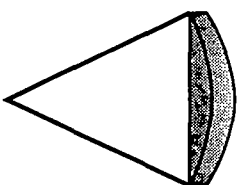





<u>Side View</u>	<u>Front View</u>	<u>Feed Impedance</u>	<u>Aperture Efficiency</u>
		(a) 400 Ω	25 %
		(b) 200 Ω	25 %
		(c) 188.4 Ω	46 %
		(d) 178.2 Ω	47.3 %
		(e) 100.0 Ω	65.2 %
		(f) 50.0 Ω	79.6 %

Figure 1.3. Prompt aperture efficiencies and feedline impedances for reflector and lens IRAs. Antennas are (a) single-coplanar- and (b) crossed-coplanar-feedline reflector IRAs, and (c) 90°-circular-conical- and (d), (e), and (f) flat-plate conical-feedline lens IRAs.

In this simple expression, all complexity is concealed in the determination of the transmission line impedance Z_{line} . Figure 1.2 shows a plot of the aperture efficiency versus feedline impedance Z_{line} and aspect ratio a/b for flat-plate TEM horns with rectangular focused apertures bounded by their electrode dimensions. We see that the lower-impedance planar TEM horns have the highest aperture efficiencies and will therefore produce the highest prompt radiated fields for a given input power and aperture area. This result is understandable because the low-impedance planar TEM horns have the most uniform fields within their apertures and the lowest field energies falling outside their apertures. Prompt aperture efficiency approaches 100 % as $a/b \rightarrow \infty$ and $Z_{line} \rightarrow 0$. However, as we will see in the next section, a close-fitting rectangular aperture is not the optimal focused aperture for a planar TEM horn.

Figure 1.3 shows computed aperture efficiencies and feed impedances for several reflector and lens IRAs. For circular-aperture antennas, η_A ranges from 25 % for reflector IRAs, with a single or crossed pair of 400 Ω feed arms, neglecting feed blockage, to 46 % for a lens IRA with an optimal 188- Ω circular-conical feed line. For rectangular-aperture lens antennas, η_A increases with increasing aspect ratio, reaching 80 % for a planar 50- Ω -feed system with $a/b = 6$. Therefore, when it is important to achieve the highest prompt aperture efficiency, a low-impedance lens IRA is preferable to a high-impedance reflector IRA.

II. Optimal Apertures

The question one might ask is “What is the most efficient focused aperture for a given feed structure?” We first imagine that such an optimal aperture exists with area A and boundary path S . We then add a small incremental area δA at some point (x', y') along S to form a new boundary path S' enclosing an area A' , as shown in Fig 2.1.

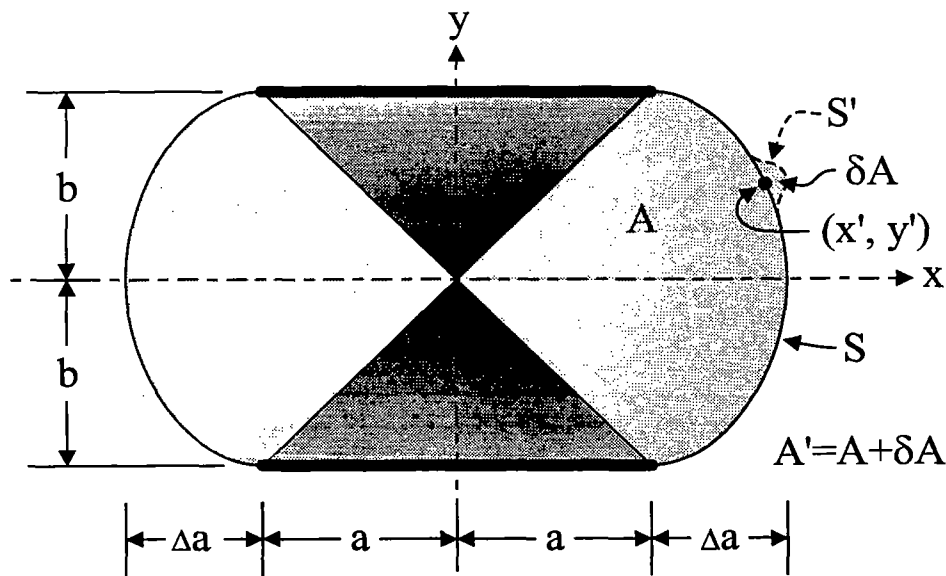


Figure 2.1. Frontal view of a focused-aperture TEM horn with optimal aperture of area A , showing a small perturbation in area δA at the boundary point (x', y') .

The new aperture efficiency $\eta_{A'}$ for the aperture with boundary S' and area A' then becomes

$$\begin{aligned}
\eta_{A'} &= \eta_A + \delta\eta_A \\
&= \frac{1}{A'} \frac{Z_{line}}{Z_{med}} \left[\frac{1}{V_{in}} \iint_{A'} E_y(x, y) dx dy \right]^2 \\
&= \frac{1}{(A + \delta A)} \frac{1}{V_{in}^2} \frac{Z_{line}}{Z_{med}} \left[\iint_A E_y(x, y) dx dy + E_y(x', y') \delta A \right]^2 \\
&= \frac{A}{V_{in}^2} \frac{Z_{line}}{Z_{med}} \left[\langle E_y \rangle + E_y(x', y') \frac{\delta A}{A} \right]^2 \left/ \left[1 + \frac{\delta A}{A} \right] \right. \quad (2.1) \\
&= \frac{A}{V_{in}^2} \frac{Z_{line}}{Z_{med}} \langle E_y \rangle^2 \left[1 + 2 \frac{E_y(x', y')}{\langle E_y \rangle} \frac{\delta A}{A} + \frac{E_y^2(x', y')}{\langle E_y \rangle^2} \frac{\delta A^2}{A^2} \right] \left[1 - \frac{\delta A}{A} + O\left(\frac{\delta A^2}{A^2}\right) \right] \\
&= \eta_A \left[1 + 2 \frac{E_y(x', y')}{\langle E_y \rangle} \frac{\delta A}{A} - \frac{\delta A}{A} + O\left(\frac{\delta A^2}{A^2}\right) \right].
\end{aligned}$$

If the original aperture were optimal, the aperture efficiency must be stationary for any incremental alteration in area δA at the boundary S . Therefore, as $\delta A \rightarrow 0$ we have

$$\delta\eta_A = \eta_{A'} - \eta_A \rightarrow \eta_A \left[2 \frac{E_y(x', y')}{\langle E_y \rangle} - 1 \right] \frac{\delta A}{A} = 0. \quad (2.2)$$

The above expression can hold only if the principal field components E_y at all points (x', y') on the boundary S obey the relationship

$$E_y(x', y') = \frac{1}{2} \langle E_y \rangle. \quad (2.3)$$

Thus, *for maximum aperture efficiency, the magnitude of the principal field component on the aperture boundary must be everywhere exactly half of the average of this field component within the aperture.* If the optimal aperture consists of several disconnected zones, then Eq. 2.3 applies to each zone with the average field and area applying to all the zones collectively.

The simplicity of Eq. 2.3 for the optimal aperture does not reflect the computational difficulties that may be encountered in trying to determine it. In general, most solutions will be found only by delicate numerical methods. One important class of problems is treated in this work: the flat-plate TEM-horn focused aperture. Although low-impedance lens IRAs achieve the highest aperture efficiencies, the lens weight can be prohibitive. By arranging smaller lens IRAs in dense arrays, the weight of lens material may be greatly reduced or even eliminated. For fixed total aperture area and antenna-element shape, the total lens mass varies inversely with the number of antenna elements. Figure 2.2 shows one possible arrangement for a dense TEM-horn-lens array. The choice of horn impedances may be limited by the source impedances and other considerations, thus limiting the aperture efficiency. However, the best arrangement for horn

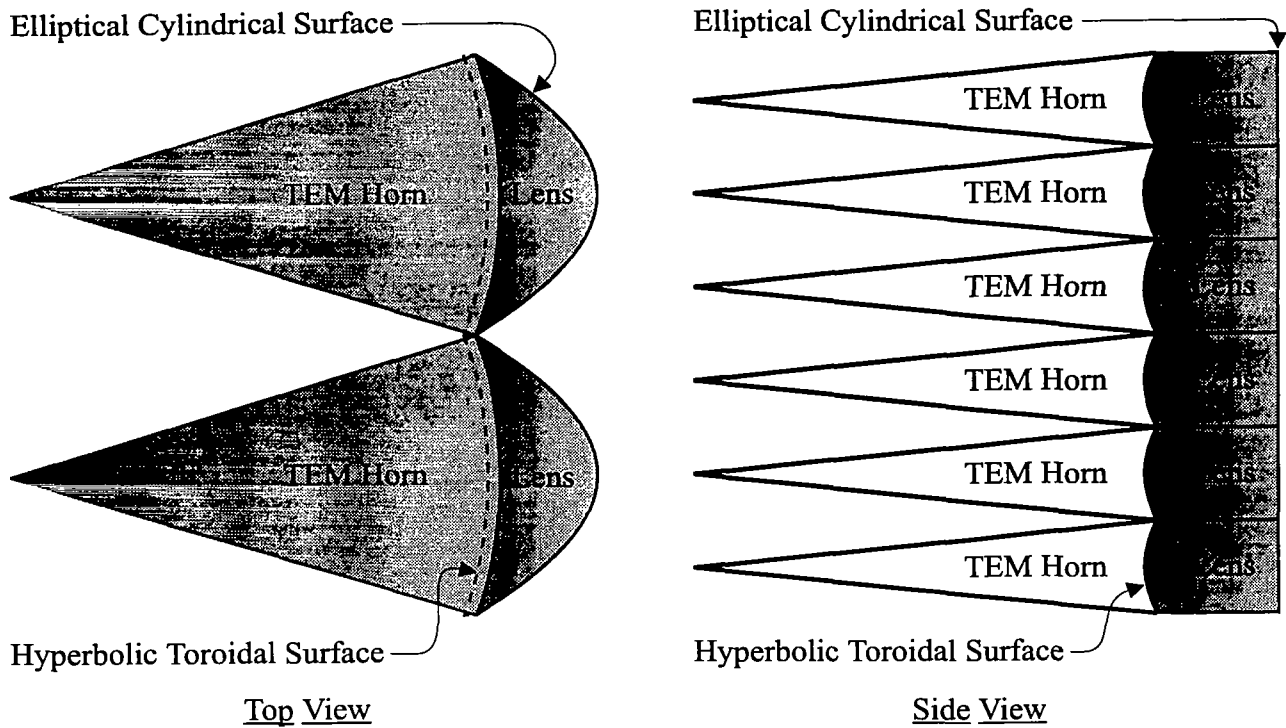
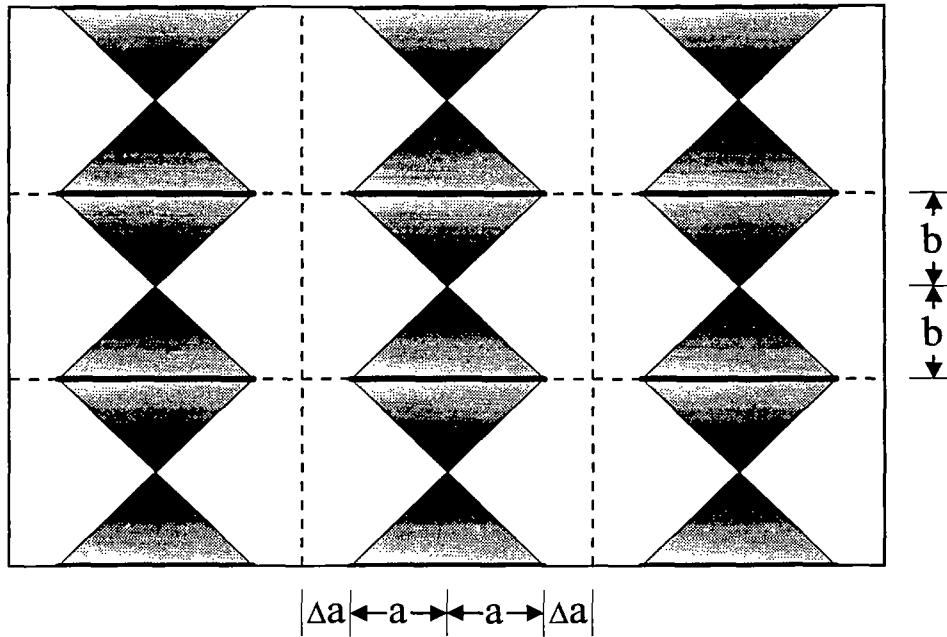


Figure 2.2. Conceptual design of a dense array of focused-aperture TEM horns with relatively low impedances and high aperture efficiencies: $Z_{\text{line}} = 86 \Omega$, and $\eta_A \cong 68\%$. All of the lens surfaces are analytic curves. For fixed total aperture area and antenna-element shape, the total lens mass varies inversely with the number of antenna elements.

placement and aperture construction within the array are yet to be determined. Figure 2.3 shows two different lattice arrangements for array construction: one with a rectangular and the other with a hexagonal unit cell and aperture shape. Note that the aperture areas of $6ab$ are 50 % greater than the areas $4ab$ within the electrode boundaries. In fact, this arrangement, with the approximate dimensions shown in Fig. 2.3, produces the highest aperture efficiencies for array elements with $a/b=1$. The aperture efficiency increases from 47.3 % for dense packing, with $\Delta a = 0$, to about 54.6 % for the less dense packing shown in Fig. 2.3, with $\Delta a \cong b/2$ for the rectangular aperture and $\Delta a \cong b$ for the hexagonal aperture.

Numerical and analytical methods outlined in Appendix A were used to derive the optimal focused apertures for flat-plate TEM horns. For a wide range of electrode aspect ratios, the aperture efficiencies and dimensions were determined for the best curved, rectangular, and hexagonal apertures. Figure 2.4 shows the three optimal apertures for an electrode aspect ratio of one ($a/b=1$). The aperture efficiencies for the optimal curved, rectangular, and hexagonal apertures were 55.3 %, 54.5 %, and 54.7 %, respectively. These aperture efficiencies are nearly the same but are noticeably larger than the 47.3 % value for the close-fitting rectangular aperture. Little is lost by choosing either the rectangular or hexagonal apertures for fitting into an array structure. The areas of the three optimal apertures are nearly the same to within 1 % for electrode aspect ratios of one or greater. This similarity results from the ideal aperture boundary lying on a curve of constant E_y .

Rectangular Aperture Array



Hexagonal Aperture Array

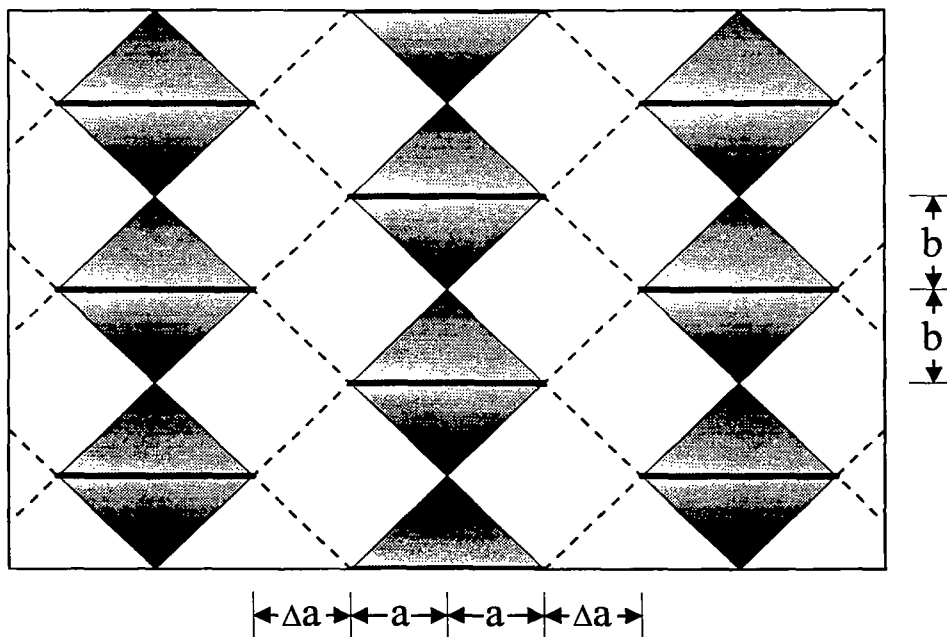


Figure 2.3. Front views of flat-plate TEM-horn arrays employing rectangular and hexagonal unit cells. For $a/b = 1$, the aperture efficiencies increase from 47.3 % for densely packed arrays with $\Delta a/b = 0$, to about 54.6 % for the less densely packed arrays shown above, with $\Delta a/b \cong 1/2$ for the rectangular apertures and $\Delta a/b \cong 1$ for the hexagonal apertures.

Optimal Apertures

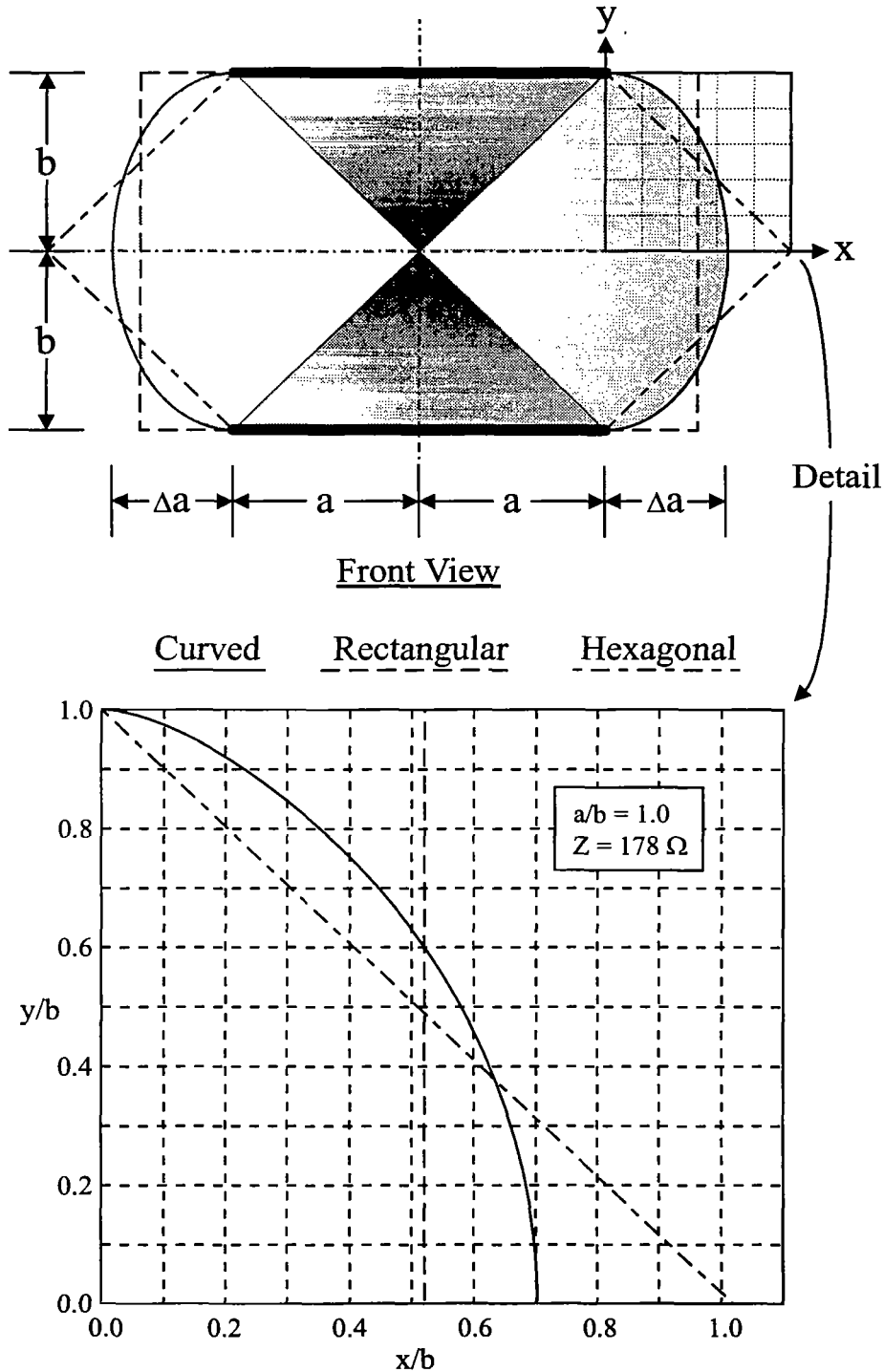


Figure 2.4. Optimal curved, rectangular, and hexagonal apertures that yield the highest aperture efficiencies for focused aperture antennas fed by flat-plate TEM horns with $a/b = 1$. The aperture efficiencies for optimal curved, rectangular, and hexagonal apertures are 55.3%, 54.5%, and 54.7%, respectively. These values compare with 47.3% for the narrow rectangular aperture with $\Delta a = 0$.

Optimal curved apertures covering the entire range of electrode aspect ratios are shown in Fig. 2.5. All curves contact the electrodes horizontally. Curves for limiting cases were derived analytically and found to lie on field lines. These curves are given by

$$y = \frac{b}{\pi} \left[\arccos\left(\frac{\pi x}{b} - 1\right) + \sqrt{1 - \left(\frac{\pi x}{b} - 1\right)^2} \right] \text{ for } a/b \rightarrow \infty, \text{ and } y = \sqrt{b^2 - x^2} \text{ for } a/b \rightarrow 0. \quad (2.4)$$

The intermediate cases were found by numerical methods described in Appendix A. Although the curves for these intermediate cases appear to lie very close to field lines, the correspondence has been shown to be inexact.³

The aperture efficiency $\eta_A(a, b, \Delta a = 0)$ of flat-plate TEM horns with narrow rectangular focused apertures bounded by their electrode dimensions is chosen as a reference function for comparison purposes. This function of a/b , which was shown in Fig. 1.2, may be computed from Eq. 1.8 and the transmission line impedance Z_{line} . The transmission line-impedance is a rather tedious function involving incomplete elliptic integrals and their inverses, and it is not easily calculated.⁴ We approximate this aperture efficiency with the sigmoidal function

$$\eta_A(a, b, 0) = \frac{a}{b} \frac{Z_{line}}{Z_{med}} = \frac{1}{1 + u_\eta (a/b)^{-k_\eta}} + \Delta\eta, \quad (2.5)$$

with $u_\eta = 1.1158$, $k_\eta = 0.8300$, and $|\Delta\eta/\eta| \leq 0.005$, for $0.01 \leq a/b \leq 10$.

Figure 2.6 presents numerically computed values of aperture efficiency $\eta_A(a, b, \Delta a)$ versus aspect ratio a/b for the three optimal aperture types (using the optimal values of $\Delta a/b$) as well as $\eta_A(a, b, 0)$ for the narrow rectangular aperture. In this plot, numerically computed values of $\eta_A(a, b, 0)$ are used instead of the values derived from Eq. 1.8 or 2.5. This is done, for the purpose of comparison, to equalize any bias caused by the numerical computational process, such as the finite plate spacing to thickness ratio, which was 60 or greater. The curves are least-squares fits to the numerically derived data points. The fitted curve for $\eta_A(a, b, 0)$ has the form given by Eq. 2.5 with slightly different coefficients ($u_\eta = 1.0938$ and $k_\eta = 0.8289$). The functional forms of the $\eta_A(a, b, \Delta a)$ curves are given by

$$\eta_A(a, b, \Delta a) = \left[1 + \frac{v_\eta}{(a/b)} \right] \eta_A(a, b, 0), \quad (2.6)$$

where the single parameter v_η was determined by a least-squares fit to the data using the numerically computed values of $\eta_A(a, b, 0)$. The values of v_η range from 0.14 to 0.16 for the three optimal apertures. The curves fit the data well with a maximum deviation of ± 0.0035 except for the three end points at very small a/b where the accuracy of the numerical method is suspect.

Figure 2.7 presents plots of computed optimal aperture edge widths Δa versus aspect ratio a/b for the three optimal aperture types. The curves are best fits to the data using sigmoidal functions of the form

Optimal Curved Apertures

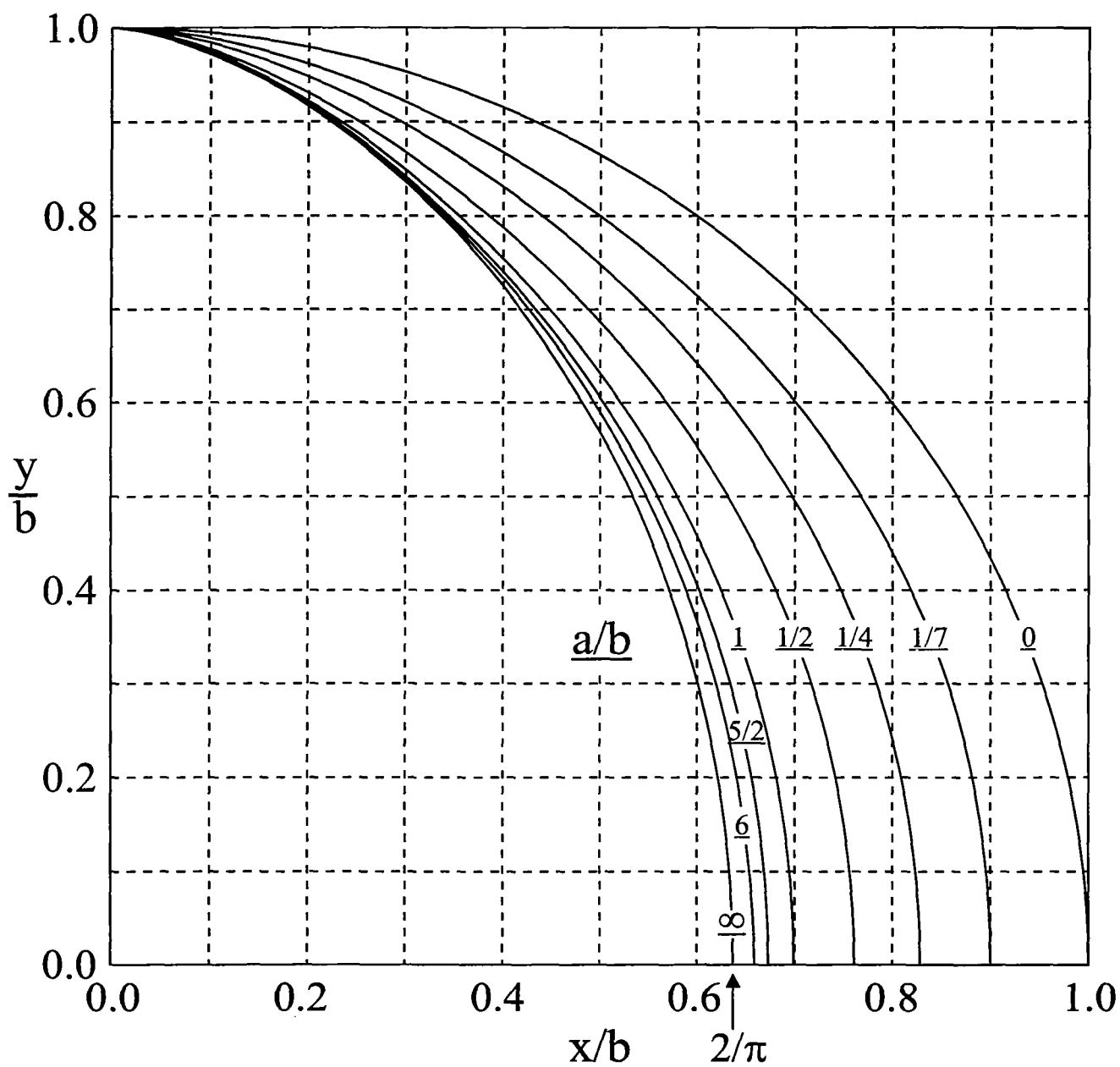


Figure 2.5. Optimal curved apertures for flat-plate TEM horns with different aspect ratios a/b and transmission-line impedances Z_{line} . Parameter sets are $(a/b, Z_{\text{line}}) = (0, \infty \Omega)$; $(1/7, 400 \Omega)$; $(1/4, 333 \Omega)$; $(0.5, 253 \Omega)$; $(1.0, 178 \Omega)$; $(2.5, 100 \Omega)$; $(6.0, 50 \Omega)$; and $(\infty, 0 \Omega)$.

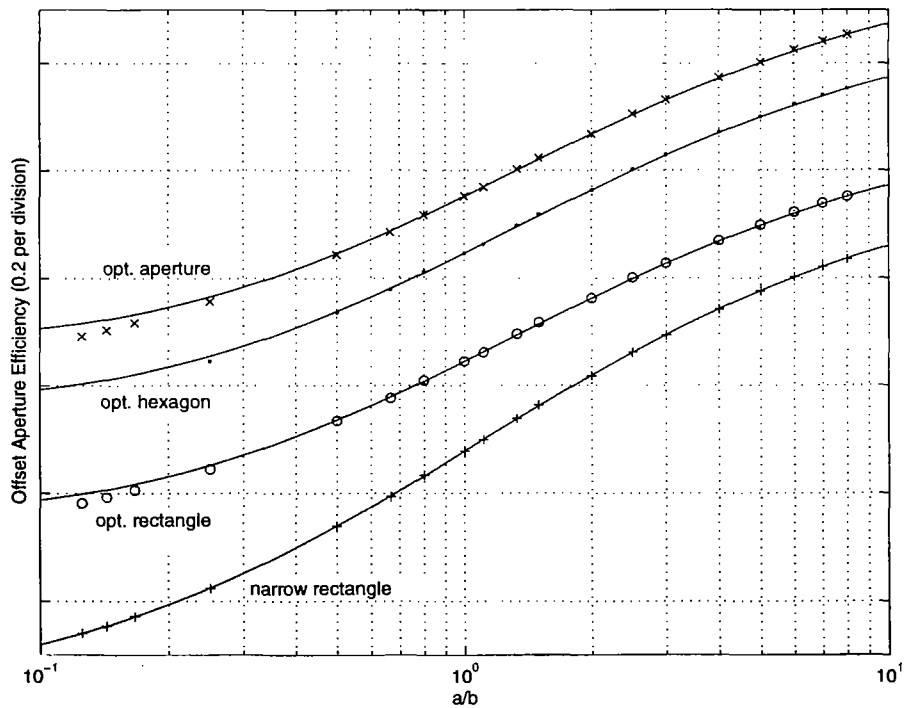
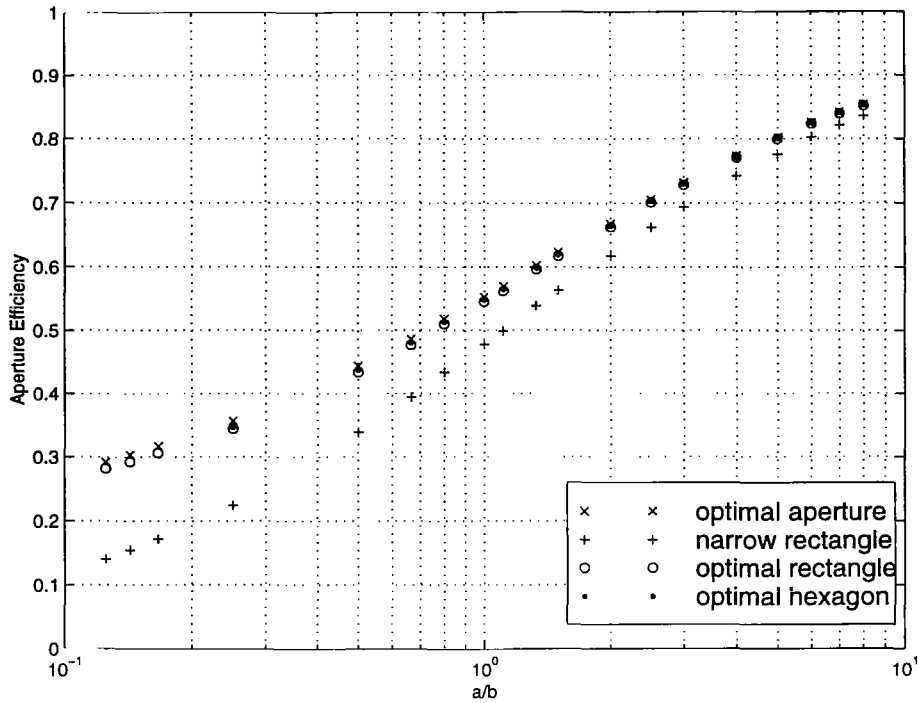


Figure 2.6. Plots of numerically computed values of aperture efficiency $\eta_A(a,b,\Delta a)$ versus aspect ratio a/b using the optimal values of $\Delta a(a/b)$ from Fig. 2.7 for the three aperture types, rectangular, hexagonal, and curved, and for the narrow rectangular aperture with $\Delta a = 0$. The lower plot shows the same data sets vertically offset along with the solid curves given by Eqs. 2.5 and 2.6 that best fit the data.

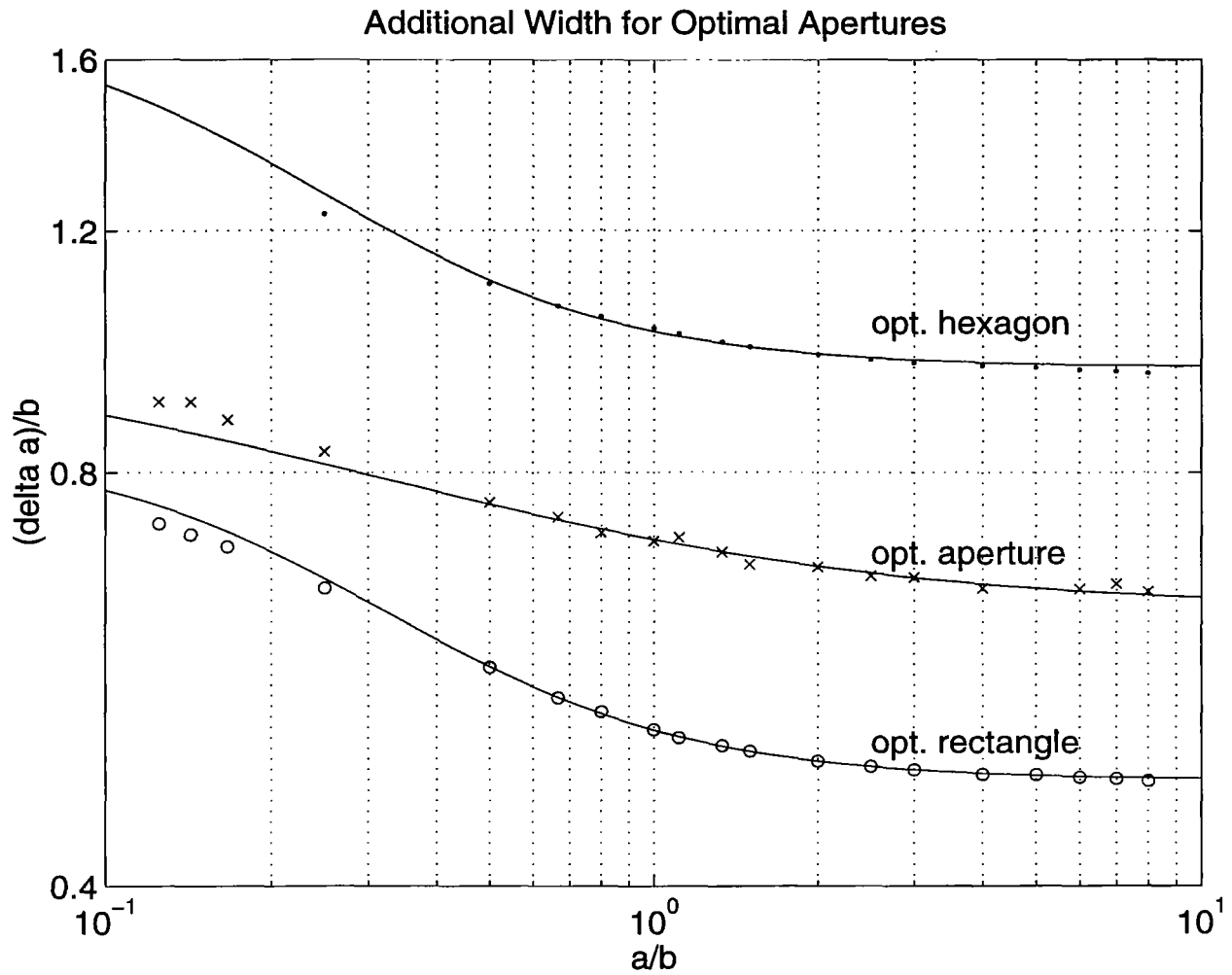


Figure 2.7. Plots of numerically computed values of $\Delta a(a/b)$ versus aspect ratio a/b that yield the maximum aperture efficiencies $\eta_A(a,b,\Delta a)$ for the three aperture types, rectangular, hexagonal, and curved. The solid curves are the functions given by Eq. 2.7 that best fit the data.

$$\log[\Delta a(a,b)] = \frac{\log[\Delta a(0,b)]}{1 + u_\Delta (a/b)^{k_\Delta}} + \frac{\log[\Delta a(\infty,b)]}{1 + u_\Delta (a/b)^{-k_\Delta}}. \quad (2.7)$$

The parameters u_Δ and k_Δ are chosen to minimize the mean-square deviation of the data, whereas the asymptotic quantities $\Delta a(0,b)$ and $\Delta a(\infty,b)$ are derived. The absolute accuracy of the fit to the data is about $\pm 1.5\%$. Equation 2.4 for the ideal curved aperture yields $\Delta a(0,b)/b = 1$ and $\Delta a(\infty,b)/b = 2/\pi$. For large a/b , the areas of the edge regions shown in Figs. 2.3 through 2.5 are the same to within 1% of that of the ideal curved aperture, which as $a/b \rightarrow \infty$ becomes $A(x \geq 0) = 3b^2/\pi$. Assuming an exact equality in this limit provides an estimate of $\Delta a(\infty,b)/b = 3/(2\pi)$ for the optimal rectangle and $\Delta a(\infty,b)/b = 3/\pi$ for the optimal hexagon. Values of $\Delta a(0,b)$ for the optimal rectangular and hexagonal apertures are obtained analytically for the limiting case as η_A and $a/b \rightarrow 0$. For the rectangular aperture as $a/b \rightarrow 0$, the leading term in the aperture efficiency is

$$\eta(a,b,z = \Delta a/b) \rightarrow \left[8\pi z \log\left(\frac{2b}{a}\right) \right]^{-1} \left[z \log\left(1 + \frac{4}{z^2}\right) + 4 \arctan\left(\frac{z}{2}\right) \right]^2, \quad (2.8)$$

which has a maximum at $\Delta a/b = z = 0.8422$, where z is the solution to the equation

$$4 \arctan(z/2) = z \log(1 + 4/z^2). \quad (2.9)$$

For the hexagonal aperture as $a/b \rightarrow 0$, the leading term in the aperture efficiency is

$$\eta(a,b,z = \Delta a/b) \rightarrow \left[2\pi z \log\left(\frac{2b}{a}\right) \right]^{-1} \left[\left(\frac{z}{1+z^2}\right) \left(\log\left(\frac{4}{1+z^2}\right) + 2z \arctan(z) \right) \right]^2, \quad (2.10)$$

which has a maximum at $\Delta a/b = z = \sqrt{3}$, where z is the solution to the equation

$$2z(z^2 - 3) \arctan(z) = (3z^2 - 1) \log[(1 + z^2)/4]. \quad (2.11)$$

The parameters used to characterize the computed data are summarized in Table 1 below.

	$\frac{\Delta a(0,b)}{b}$	$\frac{\Delta a(\infty,b)}{b}$	u_η	k_η	v_η	u_Δ	k_Δ
Narrow * Rectangle	0*	0*	1.1158*	0.8300*	-	-	-
Narrow Rectangle	0*	0*	1.0938	0.8289	-	-	-
Optimal Rectangle	0.8422*	$\sim 3/(2\pi)$ *	1.0938	0.8289	0.1411	0.1799	1.4039
Optimal Hexagon	$\sqrt{3}$ *	$\sim 3/\pi$ *	1.0938	0.8289	0.1453	0.1136	1.3907
Optimal Curve	1*	$2/\pi$ *	1.0938	0.8289	0.1568	0.3532	1.0395

Table 1. Parameter values used in Eqs. 2.5 through 2.7 to fit the numerically computed values of η_A and Δa , except where (*) denotes quantities derived from or fit to an analytic function or a derived value.

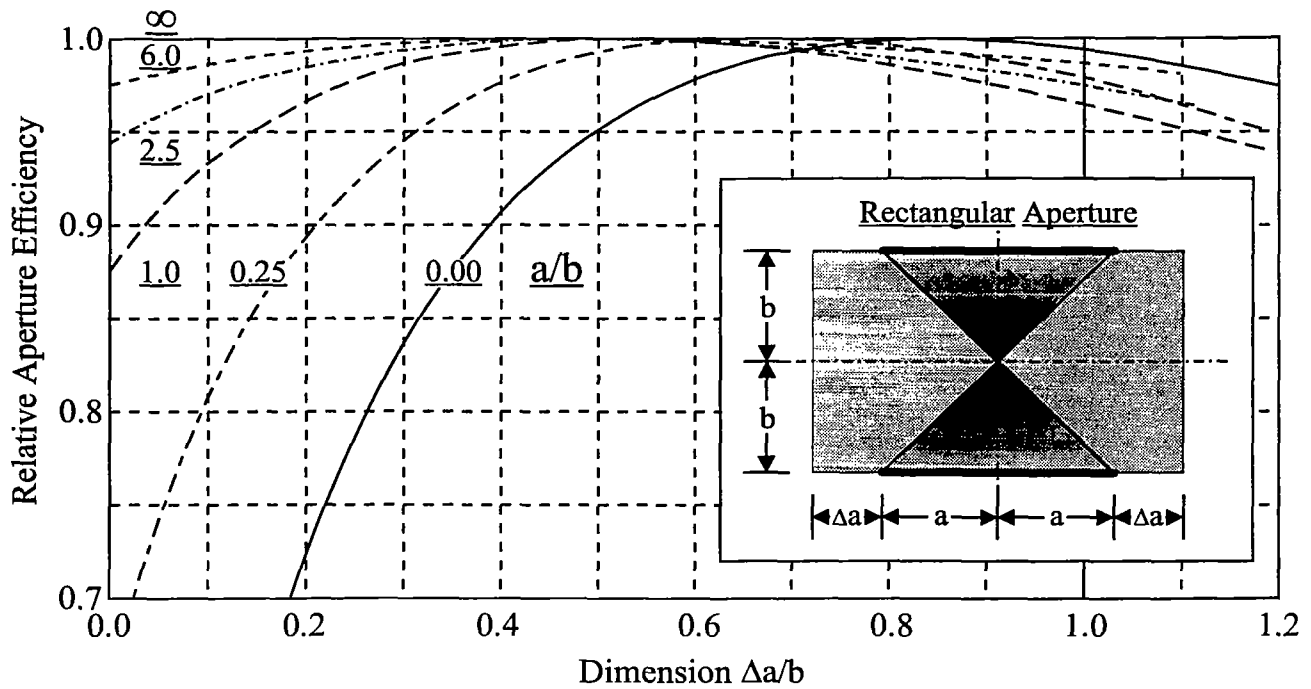


Figure 2.8a. Relative aperture efficiencies of rectangular apertures versus width parameter $\Delta a/b$ for flat-plate TEM horns with different aspect ratios a/b and transmission-line impedances Z_{line} . $(a/b, Z_{line}) = (0, \infty \Omega); (1/4, 333 \Omega); (1.0, 178 \Omega); (2.5, 100 \Omega); (6.0, 50 \Omega);$ and $(\infty, 0 \Omega)$.

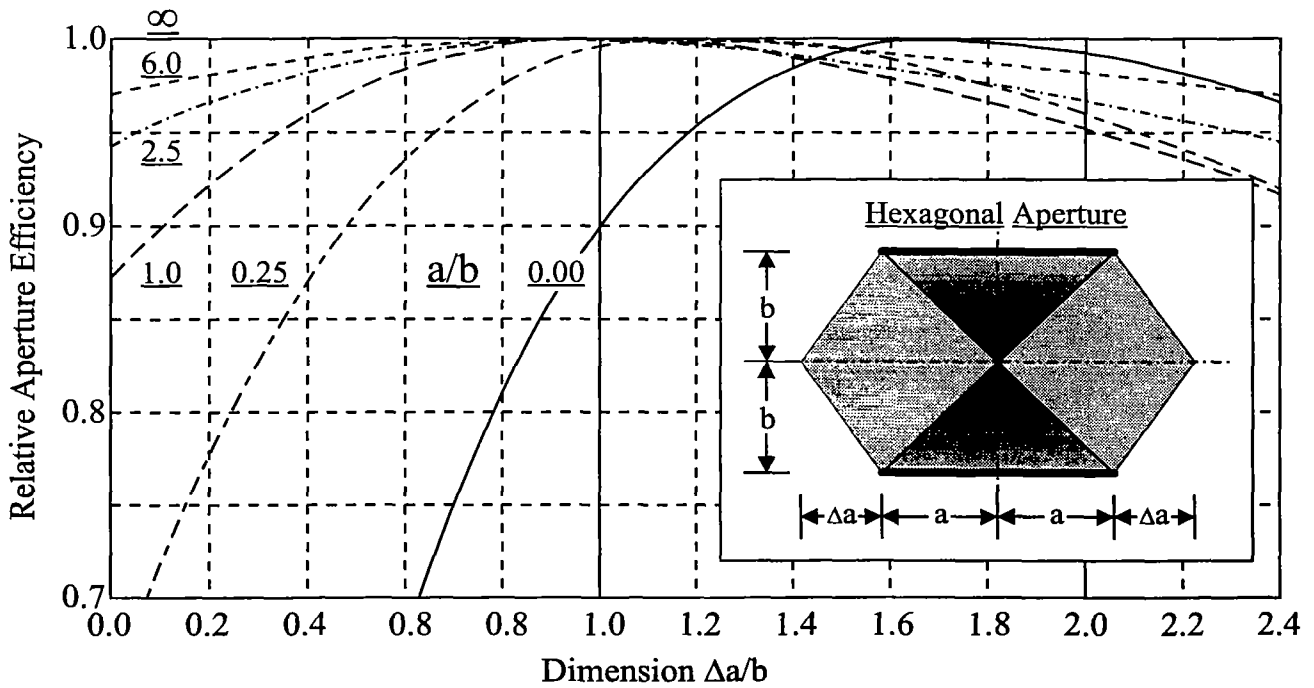


Figure 2.8b. Relative aperture efficiencies of hexagonal apertures versus width parameter $\Delta a/b$ for flat-plate TEM horns with different aspect ratios a/b and transmission-line impedances Z_{line} . $(a/b, Z_{line}) = (0, \infty \Omega); (1/4, 333 \Omega); (1.0, 178 \Omega); (2.5, 100 \Omega); (6.0, 50 \Omega);$ and $(\infty, 0 \Omega)$.

Figure 2.8 shows curves of $\eta_A(a, b, \Delta a)$ normalized to unity peak value versus $\Delta a/b$ for rectangular and hexagonal apertures. Curves generated by numerical computation cover the important impedance range from 50 to 300 Ω as well as the limiting cases as $a/b \rightarrow 0$ from Eqs. 2.8 through 2.11 and as $a/b \rightarrow \infty$. The aperture efficiency curves have rather broad peaks. The improvement in aperture efficiency achieved by optimizing Δa is greatest at the higher impedances, as might be expected. However, for the important case where $a/b = 1$, optimizing Δa increases the relative aperture efficiency by 15.4 % and the absolute aperture efficiency from 47.3 % to 54.6 %. Further increases in η_A are possible using methods described in later sections.

III. Isorefractive Media

So far we have seen that energy that falls outside the aperture is lost and can be reduced only by using lower impedance feed structures. There is another method to reduce this energy loss that utilizes isorefractive media. Isorefractive media will share the same speed of light but have different space impedances. For example

$$c_1 = \frac{1}{\sqrt{\mu_1 \epsilon_1}} = \frac{1}{\sqrt{\mu_2 \epsilon_2}} = c_2, \text{ and } Z_{med1} = \sqrt{\frac{\mu_1}{\epsilon_1}} < \sqrt{\frac{\mu_2}{\epsilon_2}} = Z_{med2}. \quad (3.1)$$

By using medium 1 in the region that illuminates the aperture and medium 2 in the region that is blocked by the aperture, the proportion of the energy blocked by the aperture is reduced. If the aperture boundary lies on E-field lines of the single-medium feedline structure shown in Fig. 3.1, the introduction of medium 2 will leave the E-fields unchanged but the H-fields reduced in medium 2. Thus, without altering the fields in medium 1, the power flow $\vec{P} = \vec{E} \times \vec{H}$ in medium 2 is everywhere reduced. The surface integral in Eq. 1.6 for η_A will be unchanged, but the transmission line impedance $Z_{line}(Z_1)$ will increase to $Z_{line}(Z_1, Z_2)$, and the dual-medium aperture efficiency $\eta_A(Z_1, Z_2)$ will be related to the single-medium aperture efficiency η_A by

$$\eta_A(Z_1, Z_2) = \frac{Z_{line}(Z_1, Z_2)}{Z_{line}(Z_1)} \eta_A. \quad (3.2)$$

The proof that such a structure is nondispersive and can support TEM-modes is outlined in Appendix B.

The circular-conical lens IRAs shown in Fig. 3.2 is often used in ultra-wideband applications. The natural aperture for this system is the circle at the edge of the lens and circular conical electrodes, which is also the boundary of self-reciprocal symmetry, which always lies on a field line.⁵ Also, for such self-reciprocal antennas, exactly half of the field energy lies outside of the circular aperture. Furthermore, the charge densities on the inner and outer surfaces of the thin electrodes are identical, and the inside and outside surfaces contribute equally to the transmission-line impedance. The aperture efficiency of this system may be increased using isorefractive media, with the higher impedance medium lying outside the circular aperture. The new aperture efficiency may be derived by inspection using Eq. 3.2, once the single-medium aperture efficiency is known.

When θ_0 is small, the prompt fields in the aperture can be approximated by the fields on a parallel transmission line with the same cross section. For the infinite transmission line, the

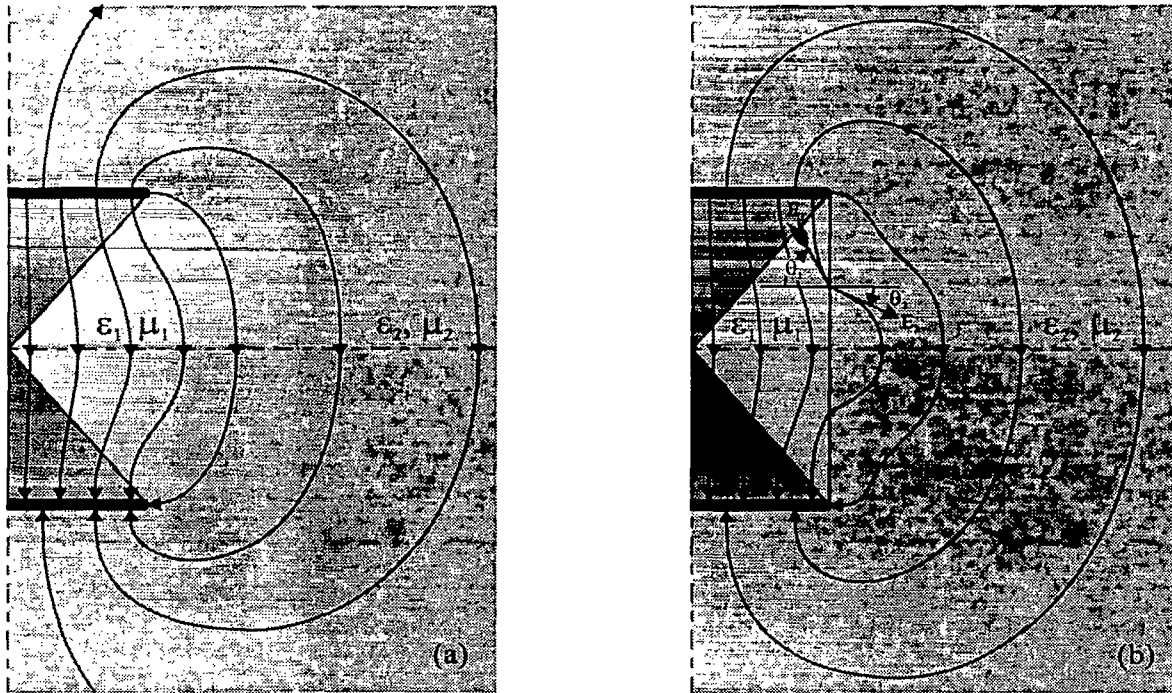


Figure 3.1. Partial field-line map of the image plane of focused-aperture TEM horns immersed in isorefractive media, when the boundary between the two media (a) does or (b) does not lie on a field line of the single-medium E-field distribution. In the latter case, the boundary fields satisfy the relations: $E_1 \sin \theta_1 = E_2 \sin \theta_2$, and $H_1 \cos \theta_1 = H_2 \cos \theta_2$, where $Z_1 \tan \theta_1 = Z_2 \tan \theta_2$. TEM modes will propagate parallel to the dielectric boundary if the isorefractive condition is met, that is $c_1 = [\mu_1 \epsilon_1]^{1/2} = [\mu_2 \epsilon_2]^{1/2} = c_2$. Aperture efficiency is enhanced if $Z_1 = [\mu_1 / \epsilon_1]^{1/2} < [\mu_2 / \epsilon_2]^{1/2} = Z_2$.

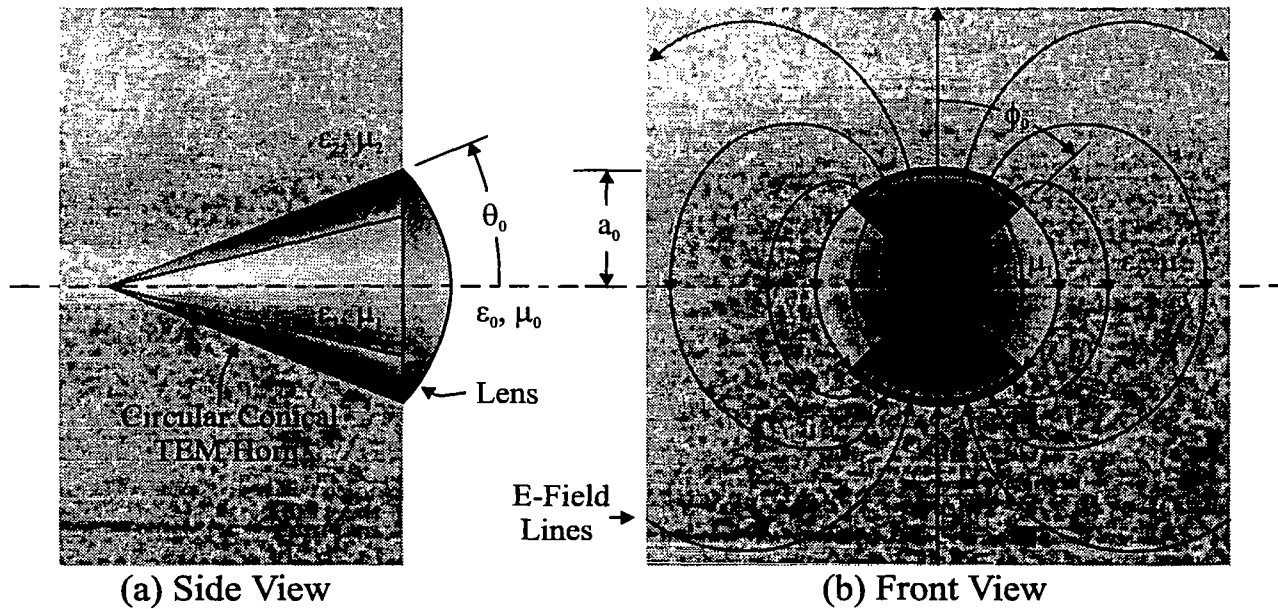


Figure 3.2. Circular conical lens IRA employing isorefractive media. The boundary between medium 1 and 2 is the circular cone containing the electrodes and the edge of the circular aperture at the edge of the lens. E-field lines are shown in the aperture plane.

three-dimensional wave equation reduces to the two-dimensional Laplace's equation in the transverse plane, and the resulting fields can be obtained by conformal transformation. The characteristic impedance of this transmission line in a single medium is⁶

$$Z_{line}(Z_{med}, m) = \frac{K(m)}{K(1-m)} Z_{med}, \quad (3.3)$$

and the aperture efficiency for the aperture defined by the circular-conical electrodes is⁷

$$\eta_A(m) = \pi \frac{Z_{line}}{Z_{med}} \left[(1 + \sqrt{m}) K(m) \right]^{-2} = \pi \left[(1 + \sqrt{m})^2 K(m) K(1-m) \right]^{-1}, \quad (3.4)$$

$$\text{with } \tan \phi_0 = \frac{1 - \sqrt{m}}{2\sqrt[4]{m}}, \text{ or } m = \left[\sec(\phi_0) - \tan(\phi_0) \right]^4, \quad (3.5)$$

where $K(m)$ is the complete elliptic integral of the first kind. Maximizing η_A with respect to m , the optimum electrode half-angle becomes $\phi_0(m) = 45^\circ$, and the optimum aperture efficiency is 46%. It was previously shown⁶ that the aperture fields are most uniform for $\phi_0 = 45^\circ$, so it is understandable that this configuration should have the highest aperture efficiency. However, even with this optimum configuration, the aperture efficiency is less than half. Half of the aperture efficiency is lost because half of the power lies outside the aperture, and the remaining 4% loss is due to the nonuniform field distribution within the aperture.

To improve the aperture efficiency, isorefractive media may be used to concentrate the power on the transmission line within the circular aperture. The modified impedance of the TEM horn due to the presence of the isorefractive media is given by taking the impedances of the two halves of the transmission line described by Eq. 3.3 in parallel:

$$Z_{line}(Z_1, Z_2, m) = \left[\frac{1}{2Z_{line}(Z_1, m)} + \frac{1}{2Z_{line}(Z_2, m)} \right]^{-1} = \frac{K(m)}{K(1-m)} \left[\frac{2Z_1 Z_2}{Z_1 + Z_2} \right]. \quad (3.6)$$

Generally the inner medium with impedance Z_1 will not be the same as free space with impedance Z_0 . Graded-dielectric antireflection coatings may be applied to the lens boundary that will operate efficiently for times appropriate to the prompt aperture-efficiency concept. Under these lossless conditions, Eq. 3.2 applies, and using Eq. 3.6 in 3.2, the two-medium aperture efficiency becomes

$$\eta_A(Z_1, Z_2, m) = \left[\frac{2Z_2}{Z_1 + Z_2} \right] \eta_A(m), \quad (3.7)$$

where $\eta_A(m)$ is given by Eq. 3.4 for a single medium. We see that by increasing Z_2 , much of the 50% loss in aperture efficiency due to power lying outside the aperture can be recovered. For $\phi_0 = 45^\circ$, the limiting value of Eq. 3.7 is 92%. The remaining 8% loss is due to nonuniform aperture filling.

Finding low-loss, nondispersive materials with arbitrary impedance and light speed is nearly impossible. It is particularly difficult to increase μ without significant loss at microwave frequencies. However, synthetic dielectrics allow a limited degree of independent manipulation of ϵ and μ . For example, using synthetic dielectrics containing suspended conducting spheres, it is possible to decrease μ by a fractional factor of about half of that by which ϵ is increased.⁸

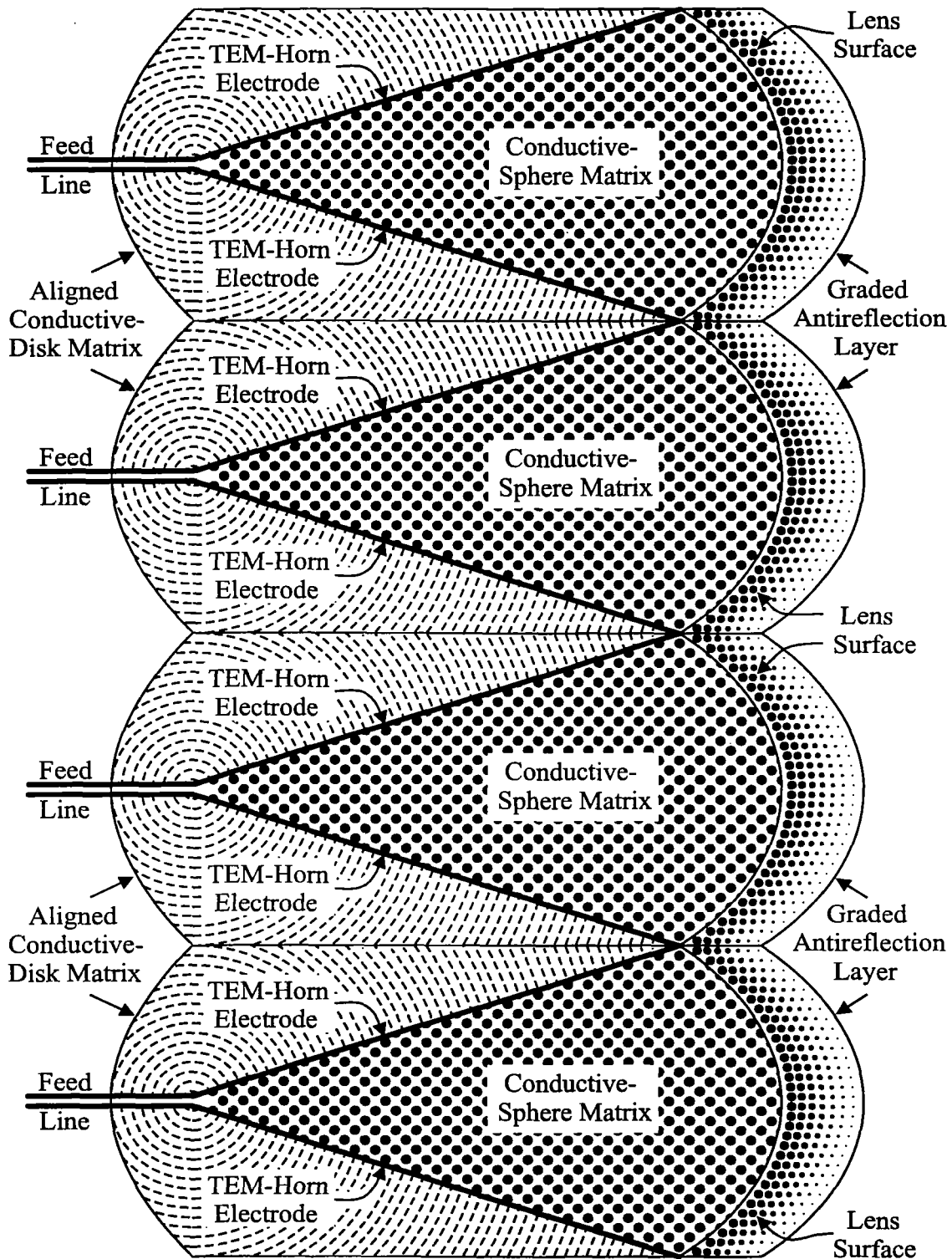


Figure 3.3. Cross-sectional view of a TEM-horn array employing isorefractive media. The inner medium is a cubic matrix of conductive hollow spheres. The outer medium is a matrix of conductive disks or strips aligned parallel to both the E- and H-fields. The broadband anti-reflection layer is a graded-index matrix of conductive spheres with spatially varying radii.

Also, ϵ may be increased without changing μ using thin metal disks aligned parallel to both the E- and H-fields. For example, if medium 1 is constructed of metal spheres in a cubic matrix having a packing fraction of 0.32 (diameters equal to 85 % of the lattice spacing) with $\mu_1 = 0.584\mu_0$ and $\epsilon_1 = 2.42\epsilon_0$, and medium 2 is a matrix of aligned metal disks with $\mu_2 \equiv \mu_0$ and $\epsilon_2 = 1.42\epsilon_0$, the media will be isorefractive with $Z_1 = 0.49Z_0$, $Z_2 = 0.84Z_0$, and $c_1 = c_2 = 0.84c$. Using these values in Eq. 3.7, the aperture efficiency increases from 46 % for a single-medium to 58 % for these synthetic media. Although the media properties are not optimized, this increase in aperture efficiency is significant, and the saving in lens weight would have a profound impact on the practicality of larger lens IRAs. Figure 3.3 shows a cross-sectional view of an array of focused-aperture TEM-horn elements using these metal-particle synthetic isorefractive media. A wideband graded-index antireflection layer is used to transition the impedance of medium one to that of free space. This is accomplished using a matrix of conductive spheres with spatially varying radii. The antireflecting behavior of this layer can be maintained for a time appropriate to the prompt-response time of the antenna elements.

One major problem remains, however. Synthetic media for time-domain applications must exhibit minimal dispersion. This can be accomplished by making the metal particles small. Smaller particles will necessarily have greater loss due to skin resistance. Whether an acceptable compromise between dispersion and loss can be found is unknown at this time. Unusual particle construction that employs special shapes and lumped-element electrical components may be required to achieve the desired results. Optimizing particle size, shape, density, composition, and lattice structure remains a topic for future work.

IV. Septum Plates

The final factor affecting loss of aperture efficiency is field nonuniformity. We have seen that low-impedance TEM horns have superior field uniformity. Improved field uniformity may be achieved with higher impedance horns by using septum plates, as shown in Fig. 4.1. The septum plates divide the aperture into zones that act as low impedance horns, which are all electrically in series. However, these interstitial plates are passive, in that they are not actively driven. They originate near the throat of the horn or within the feedline where the transmission-line approximation is valid (i.e. where transmission-line dimensions are smaller than the shortest radian wavelength of interest) and extend to the aperture plane.

If the antenna structure has strictly conical symmetry, the septum plates will carry no net charge near the aperture plane, but merely become transversely polarized in the plane in a way that makes the fields more uniform. Within each zone, the fields are more uniform, just as they are in similarly-shaped low-impedance horns. However, the field magnitudes in adjacent zones will differ in the higher impedance horns because the fields are more concentrated near the actively driven electrodes. This effect may be counteracted by allowing the plates to deviate from conical symmetry in a way that polarizes the plates longitudinally as well. This geometry alteration must occur in a region where the transmission-line approximation is still applicable, as shown in Fig. 4.1b. On the plates near the aperture plane, a net charge will then appear that compensates for the natural field gradients near the driven electrodes. This same method may be used to accomplish the opposite result, i.e. to passively roll-off the fields near the aperture edge for controlling off-boresight radiation, an action that necessarily degrades aperture efficiency.

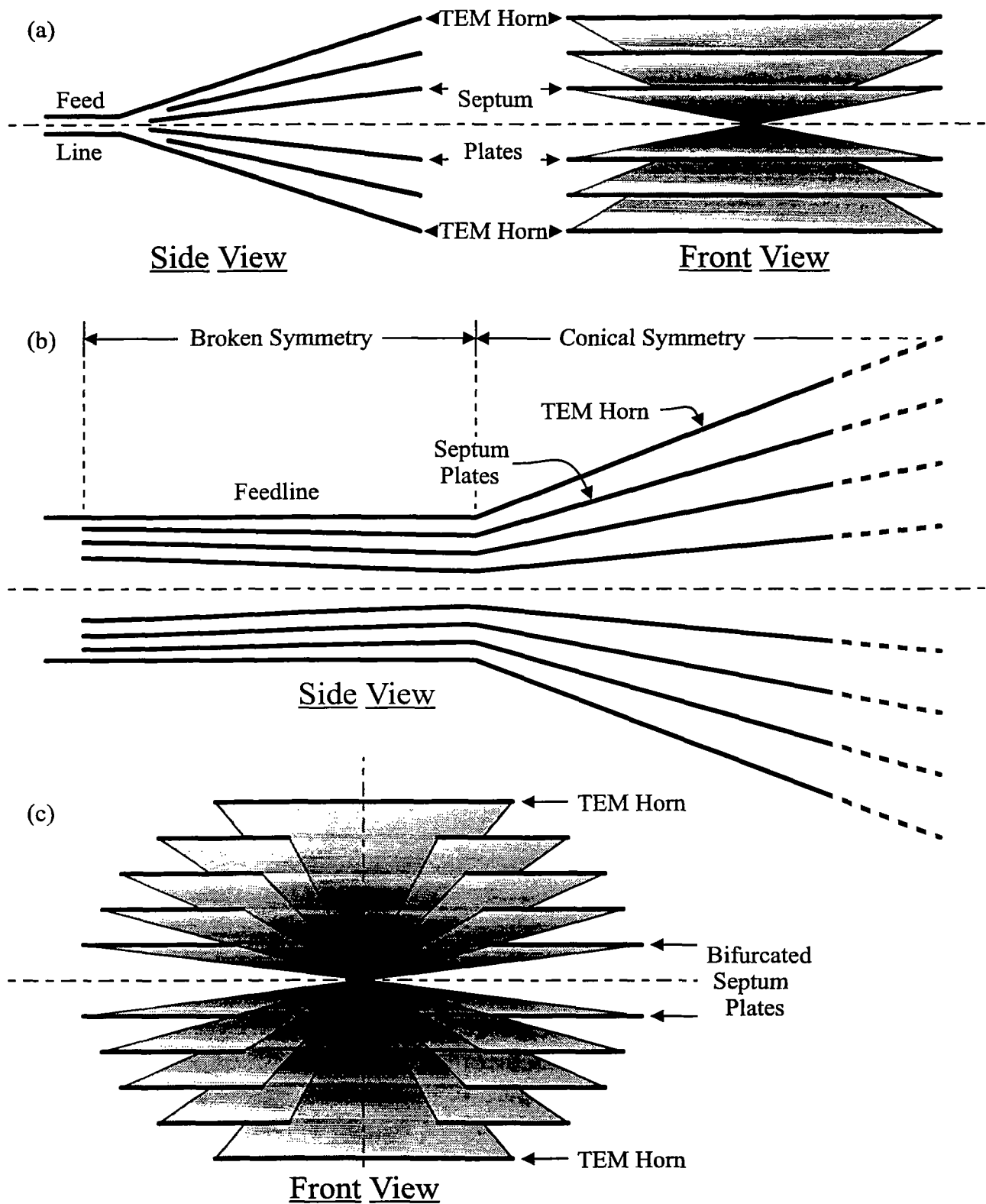


Figure 4.1. Conceptual designs of TEM horns using septum plates to improve field uniformity within the aperture. Examples include systems with (a) conically symmetric septum plates, (b) altered symmetry near feedline to modify potential distribution, and (c) bifurcated septum plates.

V. Other Considerations

There are other performance criteria used in the design of antennas and sensors for time-domain applications that can interfere with the achievement of high aperture efficiency. As mentioned earlier, control of off-boresight radiation is one. Other considerations are array-element interactions, reflected powers, resonances, and late-time responses. The aperture efficiency concept mentioned thus far pertains only to the prompt response. Controlling what follows this prompt response is a much greater task that will inevitably affect many aspects of the antenna designs. This subject is left for future work.

There is one important example of late-time response effects that has been studied. It is possible to construct E-field sensors that produce signals that precisely replicate the incident field for a finite clear time.^{9,10} They consist of TEM horns, possibly with lenses, to the front of which are added linear transmission-line extensions. The late-time aperture efficiency of these antennas can never exceed 25 %. To maintain a flat replicating response, it is not desirable that the prompt aperture efficiency be optimized in these devices. Precision replicating sensors of this type can never have high aperture efficiencies.

Antennas with high aperture efficiencies that are sustained over prolonged time scales may yet be possible to construct. Instead of maintaining the late-time response of a lens IRA with a long transmission-line extension, the response may be prolonged by using a large-aperture array, where the prompt response is maintained until effects propagate inward from the edge of the entire array rather than the edge of each element. The rudiments of a design that may approach this objective are shown in Fig. 5.1. We start with low-impedance horn elements with optimal rectangular edge regions having $\Delta a/b \cong 1/2$. At $a/b = 6$ with $Z_{line} = 50 \Omega$, the prompt aperture efficiency is a respectable 82.6 %, without having to resort to using isorefractive media or septum plates. To maintain the response at late times, the forward aperture fields must be sustained. Radiation in the backward direction would eventually occur, reducing the aperture efficiency by half. The backward radiation is prevented by the conducting back plane, and the detrimental effects resulting from the subsequent short circuiting of the array are minimized with ferromagnetic cores between the back plane and the array. High-frequency low- μ ferrites are used near the location where the horns join together. This is where the prompt interactions between the horns occur and where rapid magnetization is required. At later times, a slower high- μ magnetic material near the back plane absorbs the build-up of magnetic flux with a minimal energy expenditure. The radiated field energy blocked by the individual antenna apertures must be absorbed to prevent resonances. This is accomplished with carefully placed absorber material as well as the ferrites. Neither material should be located near the individual feed points. While prompt and late-time step responses are relatively easily to predict, the intermediate-time response, during which the E- and H-fields inside the antenna structure are evolving toward an electromagnetic equilibrium, will be very difficult to predict and will be very sensitive to the exact details of the antenna-system design. The fine tuning of this type of antenna design will most likely be accomplished by empirical and numerical methods.

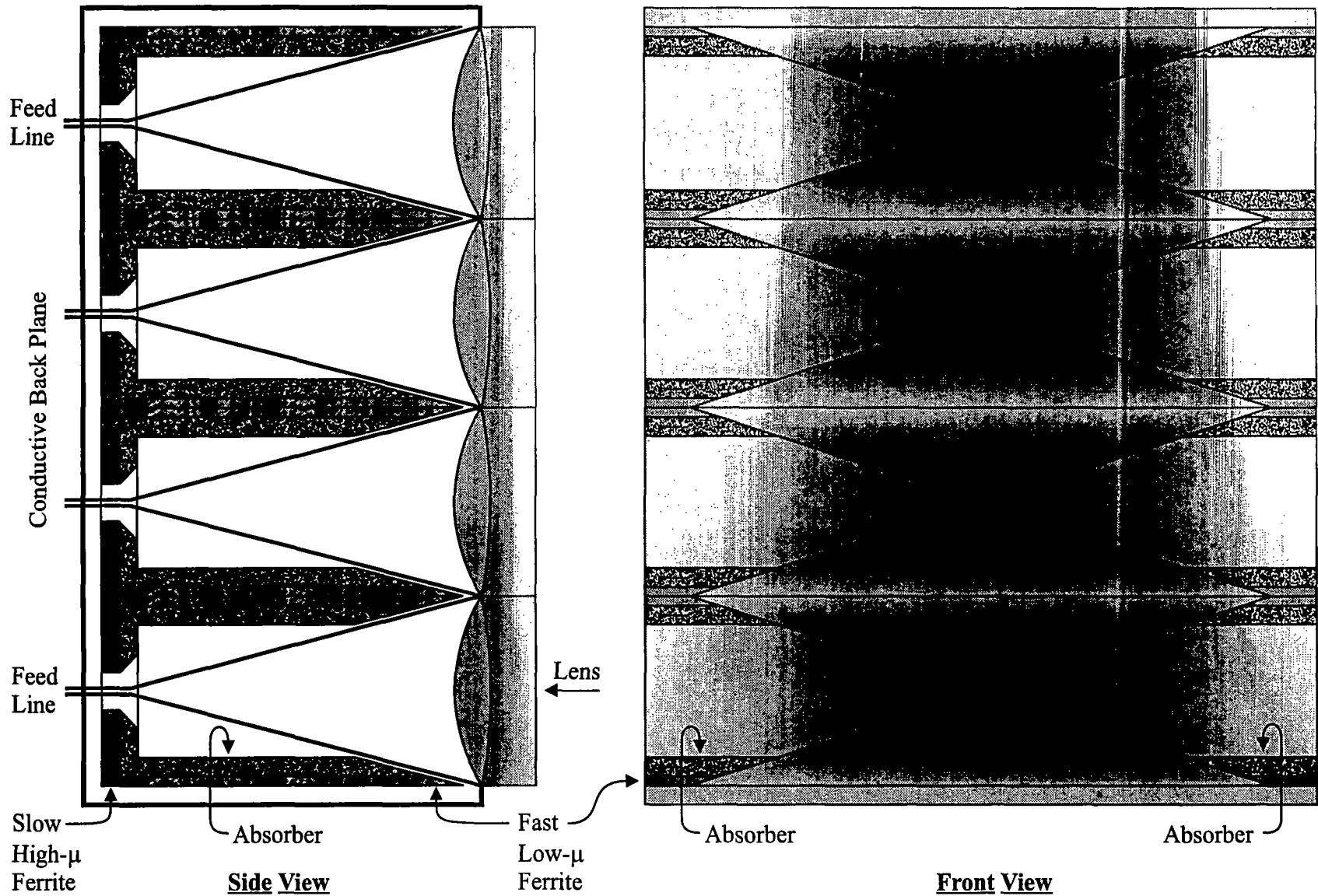


Figure 5.1. Conceptual design of antenna elements for a large TEM-horn array that can maintain a high aperture efficiency over a prolonged time scale. The array response is sustained for times comparable to the time for light to traverse the entire array rather than the individual elements. The intermediate-time response is controlled by the careful placement of absorber and ferromagnetic materials.

VI. Conclusions

The concept of aperture efficiency introduced in this report provides a quantitative measure of performance for comparing and optimizing the prompt responses of impulse radiating antennas. Aperture efficiencies can be substantially increased by choosing feed structures and aperture shapes that maximize field uniformity within the aperture and minimize energy that is blocked by the aperture. The most direct way to do this is through the use of low-impedance planar feed structures. Other methods that might be exploited utilize isorefractive media and septum plates. Antenna designs may be optimized under constraints such as restrictions on source impedance, aperture shape, off-boresight radiation, array-element interactions, and late-time responses.

Appendix A: Numerical Calculation of Aperture Efficiencies and Optimal Apertures

In order to develop computational methods that were not limited to specific cases and geometries, numerical approximations of the optimal curved, rectangular, and hexagonal apertures, and their corresponding aperture efficiencies were performed using the Matlab Partial Differential Equations (PDE) Toolbox (Version 1) running within Matlab (Version 5.1).¹¹ The PDE Toolbox is a Finite Element Method (FEM) solver that allows for efficient calculation of solutions to the elliptic equation in two dimensions, which is the general form of the Laplace Equation. This appendix is divided into three sections. Section A1 describes the general use of the PDE toolbox to solve for the field distributions in parallel-plate transmission lines of arbitrary aspect ratio. Section A2 outlines the method used to approximate the optimal curved aperture that satisfies Eq. 2.3. Section A3 covers the method used to determine the best rectangular and hexagonal apertures.

A1. Use of the PDE Toolbox for Parallel-Plate Transmission Lines

The methods described in this section are similar to those used previously to determine the current distribution in parallel-plate transmission lines.¹⁰ The principle computational difficulty is encountered in accurately modeling the unbounded transmission line geometry using a finite-sized computational domain. To overcome this problem, an iterative procedure was developed.

Definition of Problem and Mesh Generation

Because of the symmetry inherent in the problem, only one quarter of the transmission line geometry need be modeled. By replacing the symmetry boundaries where appropriate with electric and magnetic walls, the size of the problem is reduced by a factor of four. For computational reasons, the transmission line model must have finite thickness. The electrode thickness is of limited importance to the computed quantities, but it must be chosen carefully to facilitate effective computation. In practice, the electrode is made as thick as possible, while not altering the impedance of the transmission line significantly from the value for electrodes of zero thickness.¹⁰ The plate spacing to thickness ratio was 60 or greater for these computations.

The outer boundary of the computational domain is defined as a circle of radius $2\sqrt{a^2 + b^2}$. The triangular FEM mesh is created and refined using the adaptive mesh generator algorithms included in the PDE Toolbox. The boundary conditions are defined as follows: on the vertical boundary, the normal derivative of the potential is set to zero (magnetic wall); on the horizontal boundary, the value of the potential is set to zero (electric wall at zero potential); and on the electrode, the value of the potential is set to unity. While for zero-thickness electrodes, the potential boundary can be determined exactly, the finite thickness electrodes require the iterative procedure described below to accurately determine the potential on the outer boundary. The adaptive mesh algorithm generates a mesh within the domain, solves the Laplace equation numerically, and estimates the gradient of the potential (electric field) within each element. The potential gradient is compared among neighboring elements, and those triangles that have a potential gradient that differs most from the potential gradient in the neighboring cells are subdivided. Typically, the mesh was refined until there were more than 2000 elements (~ 1000 nodes). An example of an initial mesh and a mesh after refinement are depicted in Fig. A1.1.

Iterative Boundary-Condition Method

The iterative method begins with a guess as to the value of the potential on the circular outer boundary of the computational domain. A zero-order approximation to the potential on the circle is $V=0$. With this boundary condition defined, the Laplace equation is solved numerically, and the approximate charge distribution on the electrode is determined. Next, the potential is calculated at the circular boundary in an unbounded 2-dimensional space due only to this charge distribution and its images. This new potential distribution is subsequently used as the boundary condition in the next iteration. This procedure is continued until the potential on the outer boundary is stable, as determined by evaluating the mean square difference between the potential on subsequent iterations. Representative solutions for the first and final iterations are shown in Fig. A1.2.

As just described, the two algorithms are employed sequentially, i.e. the refined mesh is generated then the iterative procedure is used to determine the potential. In actuality, the iterations of the two algorithms were interspersed, i.e. the potential on the outer boundary in the $n+1^{\text{th}}$ iteration of the mesh was determined from the n^{th} charge distribution on the electrode. This method saved up to half the computational time, depending on the specific problem.

A2. Determination of Optimal Curved Apertures

In principle, determining the optimal apertures from Eq. 2.3 is straightforward. However, in practice it can be quite difficult to determine the contour that satisfies Eq. 2.3 analytically, especially in the parallel-plate transmission-line geometry, where the complex potential is defined in terms of elliptic integrals and functions of the spatial variables. For this reason, a three-step procedure was developed that allows the optimal apertures to be approximated using numerical methods.

Step 1: Approximate contours of constant E_y

The FEM gives approximate values of the potential at specific node locations within the computational domain. From these values, a piecewise linear approximation of the field can be

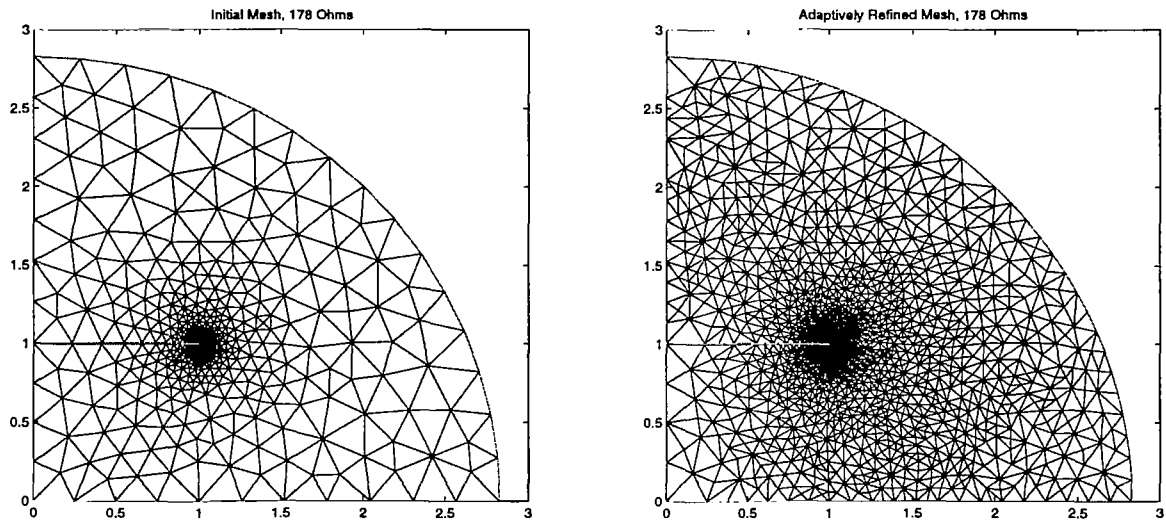


Figure A1.1. Computational domain of a $178\text{-}\Omega$ parallel-plate transmission line with (a) initial and (b) final grid mesh.

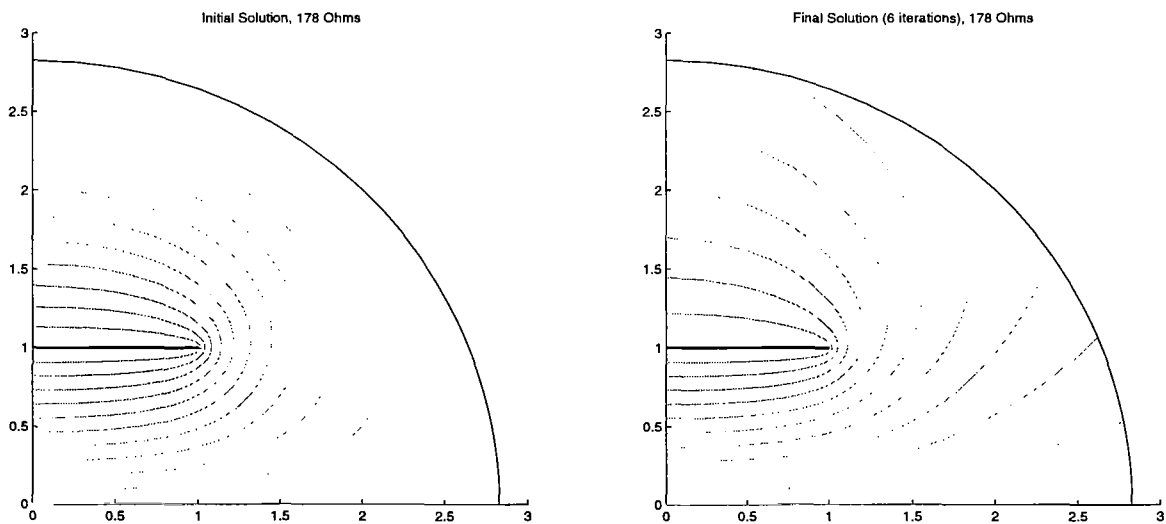


Figure A1.2. Computational domain of a $178\text{-}\Omega$ parallel-plate transmission line showing (a) initial and (b) final equal-potential surfaces.

computed. However, this approximation is difficult to work with when it comes to defining contours of constant field. For this reason, the computational domain of Fig. A1.1 was modified to that of Fig. A2.1, where artificially imposed boundaries are included in the domain. These boundaries do not affect the nature of the problem, rather they force the Matlab mesh generator to place nodes on the boundaries, allowing the user a measure of control over node placement. The specific artificial boundaries shown in Fig. A2.1 are ten radii originating at the point (1,0) and spaced 9-degrees apart from the positive x- to the positive y-directions. The vertical field was determined as a function of angle and radial distance from the point (1,0), allowing the construction of contours of constant E_y .

Even though the potentials are given at the nodes, the fields are determined at the centers of the triangular elements, and there is no way to control the placement of these centers. Therefore, the fields must be estimated at the nodes using other means. To accomplish this, a local two-dimensional quadratic form for the potential was assumed, i.e.

$$V = ax^2 - ay^2 + bxy + cx + dy + e . \quad (\text{A2.1})$$

Note that the coefficients of the x^2 and y^2 terms are equal in magnitude and opposite in sign, as required for Eq. A2.1 to satisfy the Laplace equation ($\nabla^2 V = 0$). At each node along the artificial boundaries, the coefficients in Eq. A2.1 were determined from the potential at the node and its nearest neighbors using a least-squares solution cast in the form of a singular-value matrix decomposition (SVD) for an overdetermined system. The SVD was performed using the function provided in Matlab. Once the y-component of the field was determined at each node, for each angle the radial positions corresponding to 0.3, 0.4, 0.5, 0.6, and 0.7 times the value of E_y at the origin (0,0) were estimated by linear interpolation.

Step 2: Determination of $\langle E_y \rangle$ within Constant- E_y Contours and the Optimal Aperture

With approximations for the constant- E_y contours, the second step in the process was undertaken. The computational domain of Fig. A1.1 was again modified by constructing artificial boundaries on the constant- E_y contours, as shown in Fig. A2.2. For each E_y -contour, the aperture efficiency was calculated using Eq. 1.6. The E_y -location of the aperture-efficiency maximum was estimated using a least-squares fit to a local quadratic approximation for the curve. With this value of E_y , one final mesh was defined that allowed the optimal aperture efficiency to be calculated using Eq. 1.6. An example of such a final mesh is shown in Fig. A2.3.

A3. Determination of the Optimal Rectangular and Hexagonal Apertures

The procedure used to determine the optimal rectangular and hexagonal apertures is similar to the procedure described in section A2. The computational domain of Fig. A1.1 was again modified with several artificial boundaries that were either rectangular or hexagonal in shape. The modified domains and meshes are shown in Fig. A3.1a for rectangular apertures and Fig. A3.1b for hexagonal apertures. For each aperture, the aperture efficiency was calculated using Eq. 1.6. The Δa -locations of aperture-efficiency maxima were estimated using least-squares fits to local quadratic approximations for the curves. With these Δa values, final meshes were defined that allowed optimal aperture efficiencies to be calculated using Eq. 1.6.

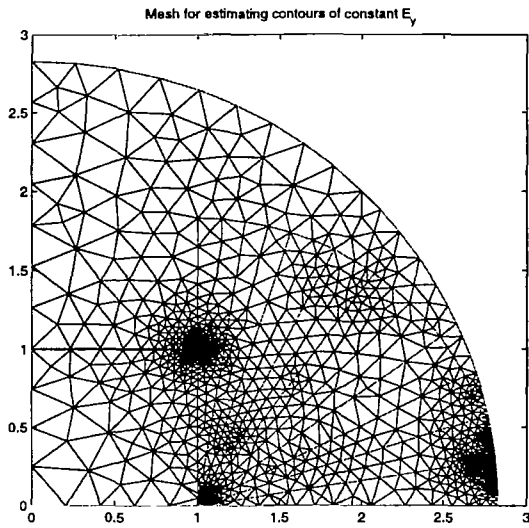


Figure A2.1. Computational domain of a $178\text{-}\Omega$ parallel-plate transmission line showing ten radial artificial boundaries emanating from the point $(1,0)$.

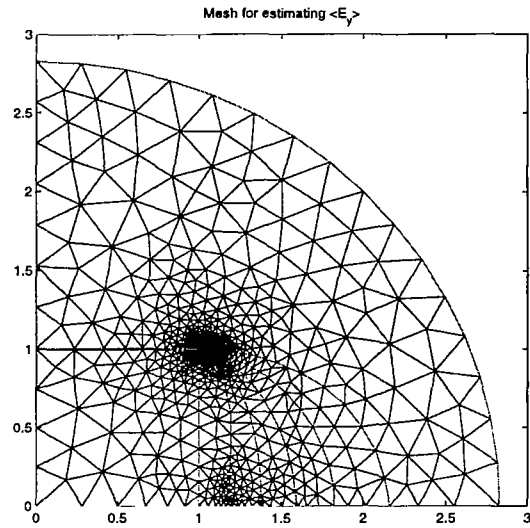


Figure A2.2. Computational domain of a $178\text{-}\Omega$ parallel-plate transmission line showing five artificial boundaries on surfaces of constant E_y .

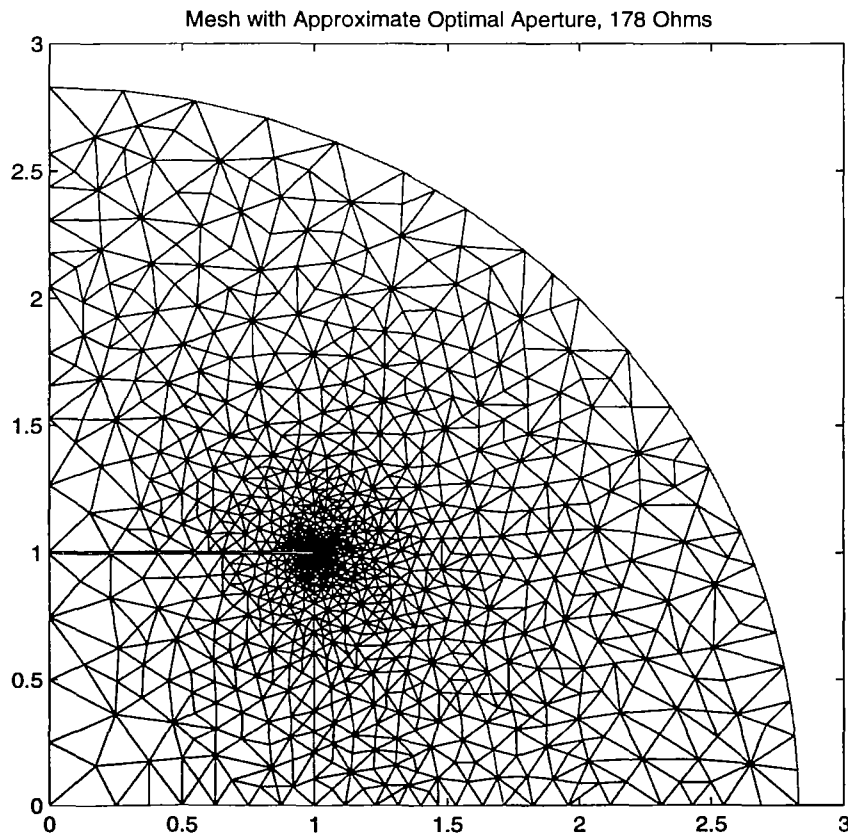


Figure A2.3. Computational domain of a $178\text{-}\Omega$ parallel-plate transmission line showing an artificial boundary at the edge of the optimal curved aperture.

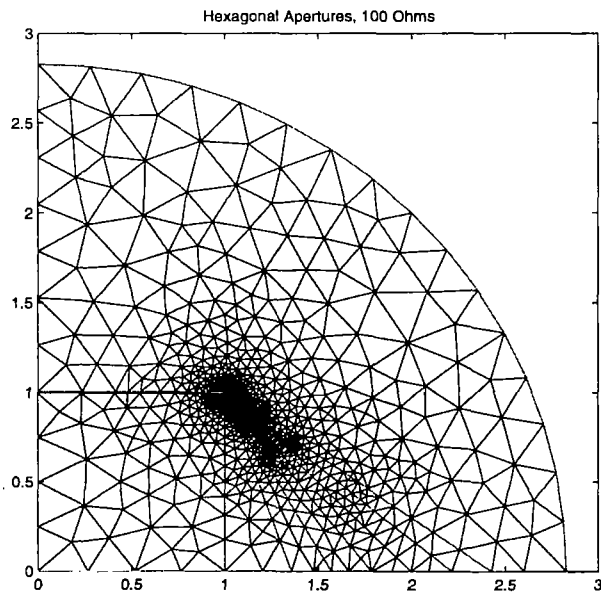
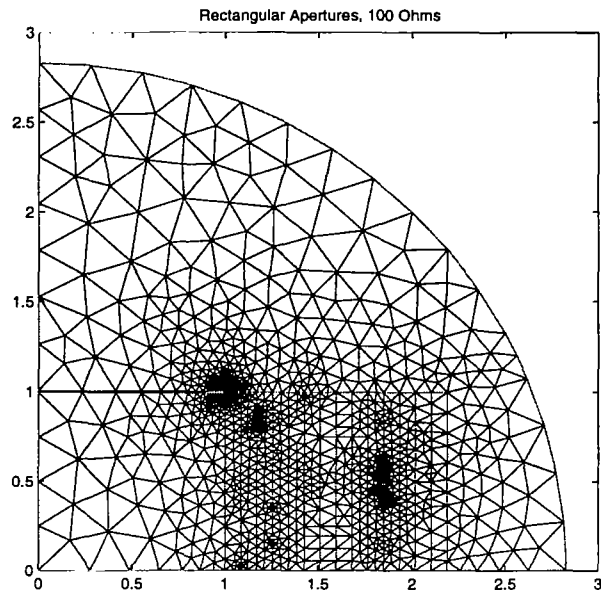


Figure A3.1. Computational domain of a $178\text{-}\Omega$ parallel-plate transmission line showing several (a) rectangular and (b) hexagonal artificial boundaries.

Appendix B: TEM-Mode Propagation in Isorefractive Media

The question to be answered is “Under what conditions will mixed isotropic dielectric media support TEM modes?” This problem has been treated in a very general way by Baum.¹² The following treatment for plane and spherical waves on linear and conical transmission lines represents special cases of the more general conditions under which TEM-waves can propagate in inhomogeneous isotropic media. For the present purposes we assume that the transmission-line structure has translational symmetry in the z -direction. The positions of electrodes and dielectric boundaries depend only upon the x and y coordinates. We assume a plane wave traveling in the positive z direction in both media to have the form

$$\begin{aligned}\vec{E}_1(x, y, z, t) &= \vec{E}_1(x, y) f_1(t - z/c_1), \text{ and } \vec{E}_2(x, y, z, t) = \vec{E}_2(x, y) f_2(t - z/c_2), \\ \vec{H}_1(x, y, z, t) &= \vec{H}_1(x, y) f_1(t - z/c_1), \text{ and } \vec{H}_2(x, y, z, t) = \vec{H}_2(x, y) f_2(t - z/c_2), \\ \text{with } E_{z1}(x, y) &= 0, H_{z1}(x, y) = 0, H_{z2}(x, y) = 0 \text{ and, } E_{z2}(x, y) = 0.\end{aligned}\quad (\text{B1})$$

In the interior of each medium, away from the boundaries, these equations satisfy Maxwell's equations for a TEM mode, such that $f_k(t)$ can be any differentiable function,

$$\begin{aligned}E_{xk} &= Z_k H_{yk}, E_{yk} = -Z_k H_{xk}, \vec{\nabla} \times \vec{E}_k(x, y) = 0, \text{ and } \vec{\nabla}^2 \vec{E}_k(x, y) = 0, \\ \text{with } c_k &= 1/\sqrt{\mu_k \epsilon_k}, \text{ and } Z_k = \sqrt{\mu_k / \epsilon_k}, \text{ for } k = 1 \text{ or } 2.\end{aligned}\quad (\text{B2})$$

Because the curl of the two-dimensional E-field $\vec{E}_k(x, y)$ is zero, this field may be derived from an electric potential function $\phi(x, y)$ that satisfies the two-dimensional Laplace's equation¹³

$$\nabla^2 \phi(x, y) = \left(\frac{\partial^2}{\partial x^2} + \frac{\partial^2}{\partial y^2} \right) \phi(x, y) = 0, \text{ with } \vec{E}(x, y) = -\vec{\nabla} \phi(x, y), \quad (\text{B3})$$

provided the electromagnetic boundary conditions can be met at the interface between the two media. We must have the parallel components of the E- and H-fields and the perpendicular components of the B- and D-fields continuous at all times and points x', y' on this boundary:

$$\begin{aligned}\vec{E}_1(x', y') f_1(t - z/c_1) \times \hat{n} &= \vec{E}_2(x', y') f_2(t - z/c_2) \times \hat{n}, \\ \vec{H}_1(x', y') f_1(t - z/c_1) \times \hat{n} &= \vec{H}_2(x', y') f_2(t - z/c_2) \times \hat{n}, \\ \mu_1 \vec{H}_1(x', y') f_1(t - z/c_1) \cdot \hat{n} &= \mu_2 \vec{H}_2(x', y') f_2(t - z/c_2) \cdot \hat{n}, \\ \epsilon_1 \vec{E}_1(x', y') f_1(t - z/c_1) \cdot \hat{n} &= \epsilon_2 \vec{E}_2(x', y') f_2(t - z/c_2) \cdot \hat{n}, \\ \text{with } \vec{B}_k &= \mu_k \vec{H}_k, \text{ and } \vec{D}_k = \epsilon_k \vec{E}_k, \text{ for } k = 1 \text{ or } 2,\end{aligned}\quad (\text{B4})$$

where \hat{n} is the normal unit vector at point x', y' on the dielectric boundary. These conditions can be met if the time-dependent wave forms are identical, and the light speeds are equal in each medium, i.e. the isorefractive condition holds:

$$f_1(t) = f_2(t), \text{ and } c_1 = 1/\sqrt{\mu_1 \epsilon_1} = 1/\sqrt{\mu_2 \epsilon_2} = c_2. \quad (\text{B5})$$

Under these conditions, a TEM mode will propagate, and the E-field distribution is found by solving the two-dimensional Laplace's equation for the transmission line in the inhomogeneous

dielectric medium. The H-field is related to the E-field through Eq. B2. The field magnitudes and the angles subtended by the E-field vectors on either side of the dielectric boundary that were shown in Fig. 3.1 are given by

$$E_1 \sin \theta_1 = E_2 \sin \theta_2, \quad H_1 \cos \theta_1 = H_2 \cos \theta_2,$$

A similar analysis holds for spherical waves in polar coordinates, where the dielectric properties depend only upon the angle coordinates. The two-dimensional electrostatics problem then becomes one of solving the Laplace equation in spherical coordinates on a spherical surface containing mixed dielectric media. This problem is more readily solved by transforming solutions of Eq. B3 in cartesian coordinates into solutions in spherical coordinates by stereographic projection.¹⁴

VII. References

1. C. E. Baum, "Radiation of Impulse-Like Transient Fields," Sensor and Simulation Note 321, USAF Phillips Lab, Albuquerque, NM, Nov. 1989.
2. W. L. Stutzman and G. A. Thiele, *Antenna Theory and Design*, pp. 395, John Wiley & Sons, Inc., New York, 1981.
3. J. S. Tyo, "Estimating the Optimum Aperture for Maximizing Prompt Aperture Efficiency in an IRA," Sensor and Simulation Note 422, USAF Phillips Lab, Albuquerque, NM, Jan. 1998.
4. T. L. Brown and K. D. Granzow, "A Parameter Study of Two-Parallel-Plate Transmission-Line Simulators of EMP Sensor and Simulation Note 21," Sensor and Simulation Note 52, USAF Phillips Lab, Albuquerque, NM, Apr. 1968.
5. E. G. Farr and C. E. Baum, "Radiation from Self-Reciprocal Apertures," in *Electromagnetic Symmetry*, C. E. Baum and H. N. Kritikos, Editors., pp. 281-308, Taylor and Francis, Bristol, PA, 1995.
6. T. K. Liu, "Impedances and Field Distributions of Curved Parallel-Plate Transmission-Line Simulators," Sensor and Simulation Note 170, USAF Phillips Lab, Albuquerque, NM, Feb. 1973.
7. J. S. Tyo, C. J. Buchenauer, and J. S. H. Schoenberg, "Use of Isorefractive Media to Improve Prompt Aperture Efficiency in a Lens IRA," IEEE Trans. Antennas and Propagat. (to be published).
8. S. B. Cohn, "Lens-Type Radiators," in *Antenna Engineering Handbook*, H. Jansik, Editor, pp. 14-22 to 14-30, McGraw-Hill, New York, 1961.

9. C. J. Buchenauer and J. R. Marek, "Antennas and Electric Field Sensors for Time Domain Measurements: an Experimental Investigation," in *Ultra-Wideband Short-Pulse Electromagnetics 2*, L. Carin, and L. B. Felsen, Editors., pp. 197-208, Plenum Press, New York, 1995.
10. C. J. Buchenauer, J. S. Tyo, and J. S. H. Schoenberg, "Antennas and Electric Field Sensors for Ultra-Wideband Transient Time-Domain Measurements: Applications and Methods," in *Ultra-Wideband, Short-Pulse Electromagnetics 3*, C. E. Baum, L. Carin, and A. P. Stone, Editors, pp. 405-420, Plenum Press, New York, 1997.
11. *Partial Differential Equation Toolbox User's Guide for use with Matlab*, The Math Works, Inc., Natic, Mass., 1995.
12. C. E. Baum, "Use of Generalized Inhomogeneous TEM Plane Waves in Differential Geometric Lens Synthesis," Sensor and Simulation Note 405, USAF Phillips Lab, Albuquerque, NM, Dec. 1996.
13. P. M. Morse and H. Feshbach, *Methods of Theoretical Physics*, pp. 13-15, McGraw-Hill, New York, 1953.
14. F. C. Yang and L. Martin, "Field Distributions on a Two-Conical-Plate and a Curved Cylindrical-Plate Transmission Line," Sensor and Simulation Note 229, USAF Phillips Lab, Albuquerque, NM, Sept. 1977.